

OMEGA/Mars Express: a new Martian atmospheric dust hunter

Yann Leseigneur^{a,*}, Mathieu Vincendon^a

^a*Institut d'Astrophysique Spatiale, Université Paris-Saclay, CNRS, Orsay, 91405, France*

ARTICLE INFO

Keywords:

Mars, atmosphere
Mars, surface
Spectroscopy

ABSTRACT

While dust is a key parameter of Mars climate, its behaviour from one year to the next can appear erratic. This variability is notably related to Global Dust Storms (GDS) which occur only certain years with different onset, duration and intensity. The interannual variabilities of the dust cycle may notably explain some characteristics of Recurring Slope Lineae (RSL), slope flows once thought to be caused by liquid water. Long-term monitoring of dust dynamics is thus required to better understand surface-atmosphere dust exchanges on Mars. Here we present a new method to detect atmospheric dust as a function of space and time in the OMEGA Near-Infrared (NIR) dataset. This dataset covers more than three Martian years; it includes the 2007 GDS which seasonality differs from the preceding (2001) and later (2018) GDS. The method is based on the decrease of the atmospheric optical path caused by dust, that can be measured by OMEGA with the $2\text{ }\mu\text{m}$ CO_2 absorption band. This measure is converted to a $0.9\text{ }\mu\text{m}$ NIR dust optical depth using notably comparisons with Mars Exploration Rovers measurements. We derive dust optical depth maps and comment on the variability of the dust seasonal cycle before, during and after the 2007 GDS. We also compare OMEGA NIR optical depths to Thermal InfraRed (TIR) ones derived by other studies. We found a NIR/TIR dust extinction optical depth ratio of 1.8 on average, with some variations notably related to dust particle size. Finally, we show in the northern hemisphere that atmospheric dust and RSL activity is correlated. This may indicate that dust lifting or transport mechanisms working at regional scale also participate to local RSL activity.


1. Introduction

Dust is omnipresent on Mars, both on the surface and suspended in the atmosphere. This high albedo material modifies solar light transfer and hence energy balance. Therefore, dust is a key parameter of the Martian climate, affecting significantly the thermal response of the surface and the circulation of the atmosphere (Smith, 2004; Geissler, 2005; Szewast et al., 2006; Kahre et al., 2013). Dust in the atmosphere is composed of mineral particles with a size distribution effective radius typically between $1\text{ }\mu\text{m}$ and $2\text{ }\mu\text{m}$ (Toon et al., 1977; Clancy et al., 2003; Wolff and Clancy, 2003; Goetz et al., 2005; Wolff et al., 2006; Clancy et al., 2010). Larger values have been reported during 2001 and 2018 global dust storms (Wolff and Clancy, 2003; Lemmon et al., 2019). Their composition appears homogeneous over the planet (Bell et al., 2000; Lasue et al., 2022) which reflects the global redistribution of dust.

The high mobility of dust leads to movements over different spatial and time scales, from sub-km to the whole planet and from minutes to several years. Dust devils are rapid and local dust movements which occur at the boundary between surface and atmosphere (Balme et al., 2003; Cantor et al., 2006). Dust storms occur at larger scales from local (i.e., $< 2000\text{ km}$) to regional extent (Martin and Zurek, 1993). In a few cases they can reach a planetary scale and form what is named planet-encircling dust events or Global Dust Storms (hereinafter GDS) (Cantor, 2007; Wang and Richardson, 2015). GDS initiation, propagation and decay can last several months (Zurek and Martin, 1993).

Most of these movements have a specific seasonality known as the Martian dust cycle. With more than 40 years of orbital observations of Mars, many features of this cycle have been characterised. A Martian Year (MY) can be divided into a "clear season" from a solar longitude (L_s ; the ecliptic longitude of the sun) of 0° to $\sim 150^\circ$ associated with an overall lower amount of atmospheric dust, and a "dust season" with a higher dust lifting activity from $L_s \sim 150^\circ$ to $\sim 360^\circ$ (Smith, 2004; Montabone et al., 2015). Local and regional dust storms are frequently observed at most latitudes during the dust season. During the clear season, some storms are still observed but mostly near the northern and southern polar cap edges (Battalio and Wang, 2021; Sánchez-Lavega et al., 2022). Some dust storms flush from one hemisphere to the other through dust storm travel routes, mainly from the northern hemisphere (Acidalia-Chryse $\sim 325^\circ\text{E}$ and Utopia-Isidis $\sim 90^\circ\text{E}$ routes, Wang and Richardson (2015); Battalio and Wang (2021)), but also from the southern hemisphere (Aonia/Solis-Valles Marineris $\sim 260-320^\circ\text{E}$ route, Battalio and Wang (2019)).

Even if several features of this seasonal dust cycle reliably repeat from one year to the next, there are still some interannual variations. The most striking change is the irregular occurrence of GDS certain Martian years. GDS can have different origins: some appear during the early dust season (near $L_s \sim 180^\circ$) such as the 2001 (MY 25) GDS (Strausberg et al., 2005; Cantor, 2007) and the 2018 (MY 34) GDS (Guzewich et al., 2019; Lemmon et al., 2019; Montabone et al., 2020), while others onset in the middle of the dust season near $L_s \sim 260^\circ$ (e.g., the 2007/MY 28 GDS, see Lemmon et al. (2015) and Wang and Richardson (2015)). These storms influence the atmospheric dynamics during the event (Bertrand et al., 2020; Montabone et al., 2020). They

 yann.leseigneur@ias.u-psud.fr (Y. Leseigneur)
ORCID(s):

are also responsible for the main modifications of the surface dust cover (Geissler, 2005; Szwast et al., 2006; Vincendon et al., 2015). However, all the formation mechanisms and consequences of GDS are not yet known precisely (Kahre et al., 2005; Newman and Richardson, 2015; Bertrand et al., 2020). We can for example wonder whether precursory signs herald GDS the season or the year before. Symmetrically, we could ask if a GDS leads to a specific dust cycle the year after due to major modifications of dust reservoirs. The impact of a GDS may also differ depending on its onset timing (early or middle of the dust season) and duration. Thus, long-term monitoring of dust dynamics may help answering these questions.

Another open question regarding the dust cycle is its precise link with Recurring Slope Lineae (hereinafter RSL). RSL, discovered by McEwen et al. (2011), are seasonal dark flows on Martian steep slopes. These features have activity phases when they appear and grow downwards more or less incrementally, and have disappearance phases when they fade (partially or totally) more or less progressively. While several studies were first conducted to investigate a possible wet origin for RSL (involving liquid water, brines, etc., see for example a review in Stillman (2018)), they are now principally explained by dry processes involving dust (Schmidt et al., 2017; Dundas et al., 2017; Schaefer et al., 2019; Vincendon et al., 2019; Dundas, 2020; McEwen et al., 2021; Munaretto et al., 2022). While their formation mechanisms are not yet precisely understood, it has been suggested that RSL could primarily be dust-removed features (Vincendon et al., 2019; McEwen et al., 2021), and that the timing of local RSL activity may be related to that of the global seasonal dust cycle (Vincendon et al., 2019). Actually, major RSL formation events occur in southern summer for all latitudes (McEwen et al., 2011; Stillman, 2018; Vincendon et al., 2019), which is also the season of main dust storms on Mars. Additionally, RSL are more abundant after a GDS decay (McEwen et al., 2021), and some RSL sites were observed to be active only after GDS (Vincendon et al., 2019; McEwen et al., 2021). In more details, RSL formation and lengthening timing however differ between northern and southern hemispheres, and between some RSL sites of a given hemisphere (McEwen et al., 2011; McEwen et al., 2014; Stillman et al., 2016; Stillman and Grimm, 2018). A more precise study of the connections between local/regional/global atmospheric dust activity, and local RSL activity, could bring additional clues to understand precisely the RSL formation mechanisms.

Several instrumental methods can be used to study dust on Mars. The dust storms are observed from Earth ground observations as far back as the early nineteenth century (observations of "yellow clouds") and were first associated with dust storms by Antoniadi (1930). Since the 1970's, different instruments were sent to Mars onboard different spacecrafts (orbiters, landers and rovers) providing key features on the dust cycle (see an overview in Smith (2008)). Visible cameras are useful from the orbit to identify dust storms and to follow their growth and their movements with

daily global imaging of Mars (Cantor et al., 2001; Cantor, 2007; Battalio and Wang, 2021). Such visible cameras are also used on rovers to measure the sun extinction and thus the atmospheric extinction optical depth as for the Mars Exploration Rovers (MER: Spirit and Opportunity) (Lemmon et al., 2015). Thermal-infrared spectrometers have been widely used from the orbit to retrieve column dust optical depths from temperature profiles (mostly at 9 μm) with nadir-observations (Smith, 2004; Montabone et al., 2015). Orbital observations of the limb with various wavelength ranges are another powerful way to constrain dust vertical distribution (Rannou et al., 2006; Smith et al., 2013; D'Aversa et al., 2022).

Two near-InfraRed (NIR hereinafter) imaging spectrometers are also present on Mars orbiters: OMEGA and CRISM which are respectively onboard Mars Express and Mars Reconnaissance Orbiter. While their main purposes are to study the surface, these spectrometers are also useful to constrain atmospheric properties as they enable composition identification (Encrenaz et al., 2005; Vincendon et al., 2011; Madeleine et al., 2012; Clancy et al., 2012). OMEGA NIR channel (named C-channel) operated over more than 3 Martian years, making it possible to explore seasonal and interannual variations of atmospheric phenomena over the whole planet. Some OMEGA studies dedicated to atmospheric dust have already been done such as: calculation of the optical depth at polar latitudes (Vincendon et al., 2007, 2008), local dust storms characterisation (Määttänen et al., 2009; Oliva et al., 2018) and vertical dust retrievals from limb observations (D'Aversa et al., 2022). However, global monitoring of the atmospheric dust has not yet been carried out.

In this paper, we develop and apply a new method to calculate atmospheric dust optical depth with the OMEGA dataset. We first present OMEGA data and the filtering criteria used in this study in section 2. Then, we detail the method to detect atmospheric dust and compute dust optical depth in section 3. Finally, we analyse in section 4 the time and spatial variations of atmospheric dust over more than 3 Martian years including the 2007 (MY 28) GDS. Summary and conclusions are drawn in section 5.

2. Data

2.1. OMEGA

We use the visible and NIR imaging spectrometer OMEGA on board Mars Express in orbit since late December 2003 (since 19 years!). OMEGA observes both the surface and the atmosphere with its nominal nadir viewing pointing geometry. The dataset is composed of hyperspectral observations with an average spatial resolution of 1 km (it varies between 0.3 and ~ 4 km depending of the Mars Express position on its elliptical orbit around Mars). The spectral range, from 0.38 to 5.1 μm , is covered by three channels (called "V", "C" and "L" channels) as defined in Bibring et al. (2004). For this study, we mainly used the C-channel (0.93-2.73 μm) which

Table 1

Description of data filtering criteria. R is the reflectance factor: $I/(F \cos(i))$. Data quality is an index (integer between 1 and 5, respectively lowest and highest quality, see OMEGA software "SOFT10" documentation for more details) that evaluates the quality of the OMEGA observations. (Note that before the orbit 1900, the data quality value 3 corresponds to 5 for the rest of the dataset.)

Description	Formulation	Detection threshold	Comments
H ₂ O(1.5 μ m)	$1 - R(1.500 \mu\text{m})/(R(1.385 \mu\text{m})^{0.7} \times R(1.772 \mu\text{m})^{0.3})$	0.01	Values > 0.01 present water ice.
Ice clouds index	$R(3.400 \mu\text{m})/R(3.525 \mu\text{m})$	0.70	Values < 0.70 present water ice clouds.
Polar cap edge	Kieffer et al. (2000); Kieffer and Titus (2001); Titus (2005)	/	3° latitude margin is added.
Incidence (i)	Data	80°	Pixels with $i < 80^\circ$ are considered.
Emergence (e)	Data	10°	Pixels with $e < 10^\circ$ are considered.
Data quality	Data	4	Data quality ≥ 4 are considered.

has been operating from 2004 to 2010¹, i.e. over more than three Martian Years (MY) notably one year before (MY 27), during (MY 28) and after (MY 29) a Global Dust Storm (hereinafter GDS). This dataset contains 9646 observations and covers almost the entire Martian surface with repeated observations available for most places. The L-channel (2.53–5.1 μ m) is also used to compute spectral indexes defined in the following section.

OMEGA data are handled using the Python module “OMEGA-Py” freely available on GitHub at <https://github.com/ASTcherbinine/omegapy>.

As detailed in the next sections, our study relies on the quantification of the variability of the atmospheric 2 μ m carbon dioxide (CO₂) absorption as a function of atmospheric dust content. This band has been already used by Forget et al. (2007) and Spiga et al. (2007) to compute the pressure at the surface from the Martian orbit.

2.2. Data filtering

We have applied different filters to select observations relevant for our study and to remove artefacts. The definitions and thresholds of these filters are detailed in table 1. Most criteria are routinely used while handling the OMEGA dataset, and have been previously described (Ody et al., 2012; Vincendon et al., 2015).

We pay here a particular attention to data properties that may impact the 2 μ m range. In particular, transient H₂O or CO₂ ice at the surface or in the atmosphere that can create a spectral signature at 2 μ m that may modify the quantification of the CO₂ gas band depth. Firstly, we remove observations above or near the seasonal polar caps. The position of ice cap edges changes with season: we evaluate ice spatial extent using thermal infrared data of the northern (Kieffer and Titus, 2001) and southern hemisphere (Kieffer et al., 2000; Titus, 2005). We exclude areas corresponding to the caps, with a 3° equatorward latitude margin. Additionally, we identify water ice (clouds or frost) based on the 1.5 μ m water ice band (Langevin et al., 2007). A conservative threshold of

1% is considered (this may remove observations that actually do not contain ice). An additional water ice criteria based on the 3 μ m band is also used (Table 1) as it can help to detect some clouds (Langevin et al., 2007; Madeleine et al., 2012; Audouard et al., 2014).

Then we filter data depending on their viewing geometry. We consider only near nadir observations (emergence angle $e < 10^\circ$) with an incidence angle (i) lower than 80° to simplify optical path modelling in the next sections. As most OMEGA observations is compliant with these restrictions, this only weakly impact the amount of usable data.

3. Method

3.1. Overview

We have developed a method to identify atmospheric dust based on the 2 μ m CO₂ gas absorption band. The depth of this band depends on the distance travelled by the sun’s rays through the atmosphere mainly composed of this gas ($\sim 96\%$). Indeed, in a clear atmosphere, with a low atmospheric dust load, the sun’s rays reach the surface where they are reflected towards the instrument (Figure 1, panel A). As represented in panel C of Figure 1, the 2 μ m band corresponding to this situation (in blue) is deep. However, when there is a high atmospheric dust load, the sun’s rays are reflected on the atmospheric dust. Thus, the distance travelled in CO₂ is shorter, as we can see in panel B of Figure 1, and the corresponding band is therefore less deep (red band in panel C). Note that a method presenting some similarities has been previously suggested with the 2.7 μ m CO₂ band, which differs from the 2 μ m one as it saturates to 0 without atmospheric dust (Titov et al., 2000).

In the next sections, we quantify this modification of the CO₂ optical depth by comparing the observed optical depth ($\tau_{\text{CO}_2, \text{obs}}$) of a given OMEGA observation to the theoretical one for a clear atmosphere ($\tau_{\text{CO}_2, \text{pred}}$). The resulting difference is $\Delta\tau_{\text{CO}_2}$ (equation 1).

$$\Delta\tau_{\text{CO}_2} = \tau_{\text{CO}_2, \text{pred}} - \tau_{\text{CO}_2, \text{obs}} \quad (1)$$

¹We can notice that V-channel and L-channel are still operating at the time of writing of this article.

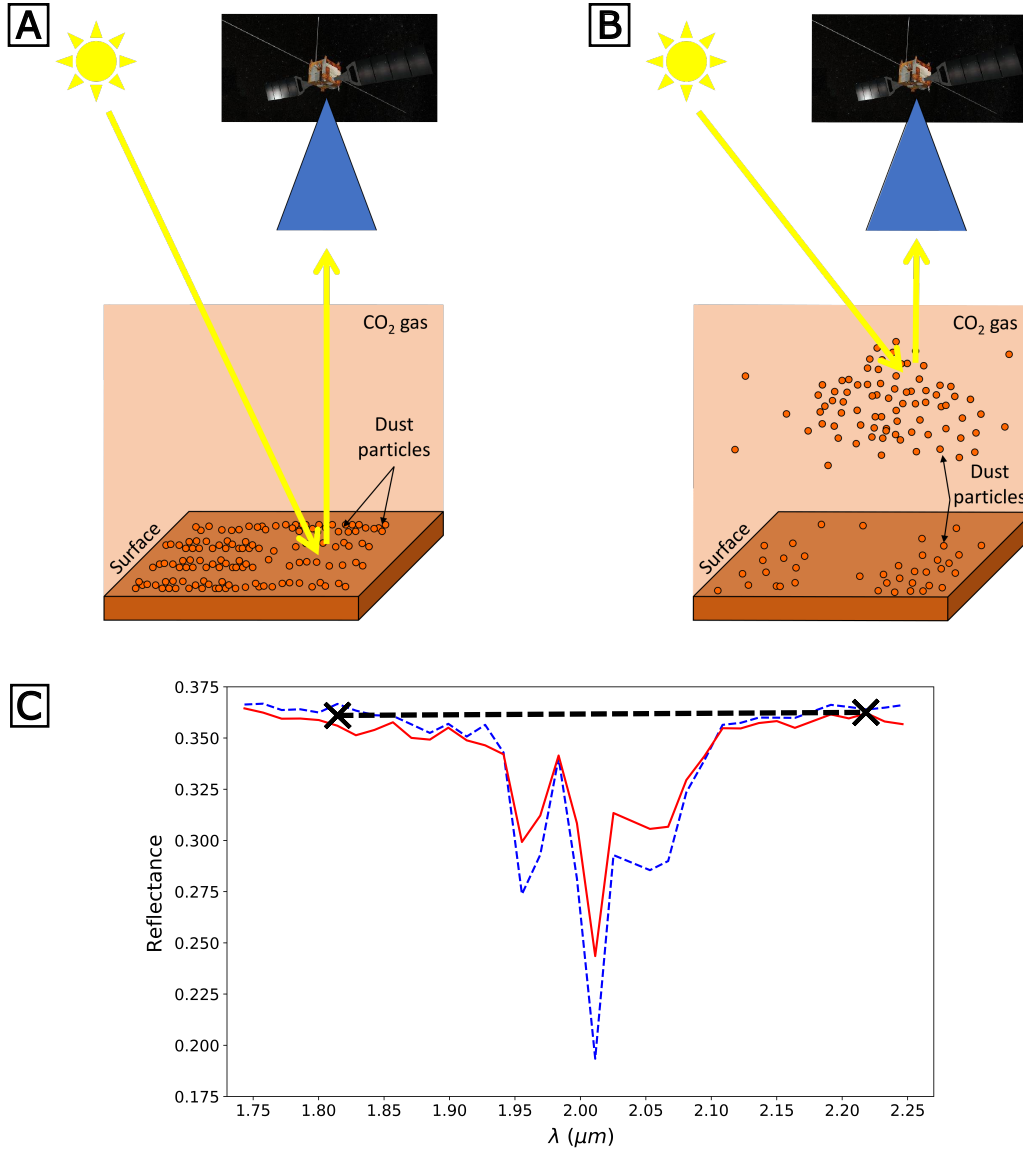


Figure 1: Overview of the method used in this paper to detect dust in the atmosphere. (Top) schemes illustrating photon paths in the atmosphere in case of low [A] and high [B] atmospheric dust load. [C] represents the corresponding 2 μm CO_2 absorption bands (clear atmosphere: dashed blue line; dusty atmosphere: red line). The band is shallower in a dusty atmosphere than in a clear one. The (linear) continuum used for band depth calculation is represented by a black dotted line: it is defined between wavelengths 1.82 μm (average of 1.80 μm and 1.84 μm) and 2.22 μm symbolised by black crosses.

This quantity will then be related to the optical depth of atmospheric dust τ_{dust} using a calibration procedure based on ground truth measurements provided by the Mars Exploration Rovers (equation 2).

$$\tau_{\text{dust}} = f(\Delta\tau_{\text{CO}_2}) \quad (2)$$

3.2. Calculation of CO_2 optical depths

We compute the observed CO_2 optical depth for a given OMEGA pixel at 2 μm ($\tau_{\text{CO}_2, \text{obs}}$) using equation 3, where $R(2.01 \mu\text{m})$ is the reflectance factor at 2.01 μm and R_0 is the reflectance factor of the continuum (see panel C of Figure 1 for details).

$$\frac{R(2.01 \mu\text{m})}{R_0} = e^{-\tau_{\text{CO}_2, \text{obs}}} \quad (3)$$

We estimate the predicted CO_2 optical depth when the atmosphere is clear ($\tau_{\text{CO}_2, \text{pred}}$) using the following approach. The optical depth depends on the amount of gas encounter by the photons as they pass through the atmosphere. Firstly, in the simple case of normal incidence rays ($i = 0^\circ$), the CO_2 optical depth is proportional to the pressure P (equation 4). We note α the proportionality factor which depends notably on OMEGA instrumental response and cannot be simply inferred.

$$\tau_{CO_2, pred} = \alpha P \quad (4)$$

For other incidence values, the geometrical path of the sun's rays should be $1 + 1/\cos(i)$. However, a small amount of dust is always present in the atmosphere of Mars, even during the clear atmospheric season. As a consequence, the actual optical path will slightly depart from this law. We take this into account by adding an exponent $d < 1$ to the term $1/\cos(i)$ (see equation 5).

$$\tau_{CO_2, pred} = \alpha P \times \left(1 + \left(\frac{1}{\cos(i)}\right)^d\right) \quad (5)$$

The presence of residual atmospheric dust when the atmosphere is clear will also result in the fact that $\tau_{CO_2, pred}$ is a function of surface albedo. Indeed, the average atmospheric optical path measured from the orbit depends on the relative weight of photons reaching the surface and then scattered (long path), versus photons directly scattered by dust before reaching the surface (shorter path). In the following "albedo" will refer to the reflectance factor at $2.26 \mu\text{m}$ (this wavelength is located outside the $2 \mu\text{m}$ band, it is used to estimate the reflectance level of the surface at $2 \mu\text{m}$). Overall, $\tau_{CO_2, pred}$ is thus expected to be describable by equation 6, where $f(\text{Alb})$ is an unknown albedo function.

$$\tau_{CO_2, pred} = \alpha P \times \left(1 + \left(\frac{1}{\cos(i)}\right)^d\right) \times f(\text{Alb}) \quad (6)$$

In the next section, we calibrate the unknown parameters α , d and $f(\text{Alb})$ of equation 6.

3.3. Calibration of clear atmosphere CO_2 optical depth

We made a selection of 57 OMEGA observations (see Table 2) to calibrate equation 6. As $\tau_{CO_2, pred}$ corresponds to clear atmospheric conditions, we have selected data corresponding to expected low optical depths according to previous studies (Smith, 2004; Lemmon et al., 2015). These selected observations cover various altitudes and seasons, sampling all expected Martian pressures. Similarly, we have selected observations at various solar incidence angles and surface albedos, useful to characterise these two other dependencies of $\tau_{CO_2, pred}$.

Firstly, we characterised the albedo dependency of $\tau_{CO_2, pred}$ using three observations for which albedo varies strongly while other variables (pressure and incidence) are nearly constant (variations respectively less than 10 Pa and less than 3° , see Table 2). We show in Figure 2 how the observed CO_2 optical depth changes with albedo. We observe that variations are lower than $\pm 5\%$. We use these observations to estimate the expression of $f(\text{Alb})$ (equation 7) and its parameter values (see Table 3).

$$f(\text{Alb}) = \frac{A_{max}}{1 + \left(\frac{A_{max}}{A_0} - 1\right)e^{-k \times \text{Alb}}} \quad (7)$$

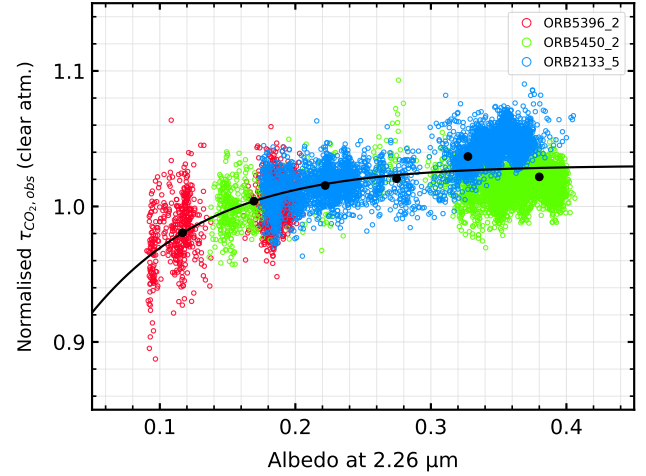


Figure 2: Calibration of the albedo dependence $f(\text{Alb})$ of $\tau_{CO_2, pred}$ (equation 6). $f(\text{Alb})$ (solid black line, equation 7) is constrained using observed variations of clear atmosphere CO_2 optical depth (normalised) as a function of albedo, derived from 3 OMEGA observations (colored dots). Other variables (incidence and pressure) are constant in each observation. Median values are computed on albedo ranges of 0.06 width (black circles) to better constrain the fit.

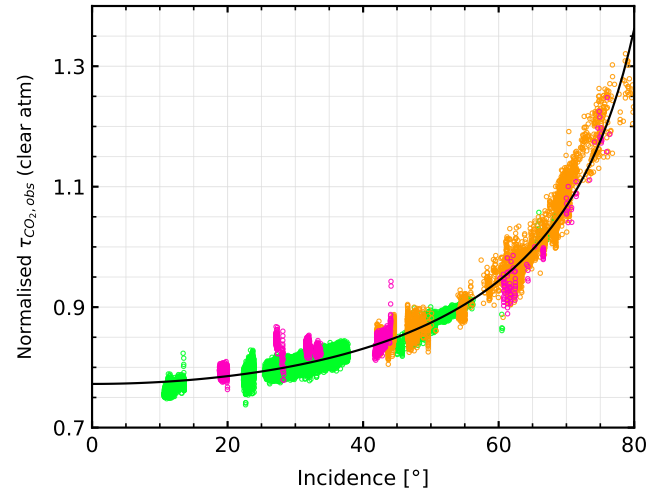


Figure 3: Calibration of the incidence dependency of $\tau_{CO_2, pred}$ (equation 6). This graph represents the observed CO_2 optical depth (normalised) as a function of incidence. 34 OMEGA observations for three different pressure and albedo ranges are used, respectively: [500, 510] Pa and [0.35, 0.45] (pink points), [720, 730] Pa and [0.35, 0.45] (green points), [485, 495] Pa and [0.25, 0.30] (orange points). An incidence exponent $d \approx 0.53$ in equation 6 provides a satisfactory fit with the data (solid black line).

Secondly, we use 34 observations covering a large incidence range to estimate the value of the exponent d (equation 6). Other variables (pressure and albedo) are nearly

Table 2

OMEGA calibration data used to characterise the three CO₂ optical depth dependencies with the corresponding range widths for each one (∀: all values are considered).

Dependency	Cubes	Pressure range	Albedo range	Incidence range
Albedo	2133_5, 5396_2, 5450_2	$\Delta P \leq 10$ Pa	∀	$\Delta i \leq 3^\circ$
Incidence	0049_0, 0097_0, 0103_3, 0243_3, 0248_2, 0308_2, 1170_3, 1533_2, 2432_0, 2436_1, 2526_1, 3639_2, 5398_2, 5450_2, 6486_5, 7267_3, 7287_3, 7287_4, 7288_2, 7290_3, 7290_4, 7294_3, 7303_3, 7306_4, 7310_2, 7324_3, 7327_3, 7330_3, 7334_3, 7365_3, 7366_4, 7370_3, 7393_4, 7422_3	$\Delta P \leq 10$ Pa	$\Delta Alb \leq 0.10$	∀
Pressure	0049_0, 0097_0, 0103_3, 0243_3, 0248_2, 0270_3, 0286_3, 0308_2, 1143_3, 1150_3, 1170_3, 1183_3, 1238_2, 1510_5, 1533_2, 2133_5, 2245_4, 2256_4, 2432_0, 2436_1, 2526_1, 3198_3, 3220_1, 3262_2, 3345_2, 3639_2, 3674_2, 3685_2, 5396_2, 5398_2, 5450_2, 5692_2, 5814_2, 6486_5, 7267_3, 7287_3, 7287_4, 7288_2, 7290_3, 7290_4, 7294_3, 7303_3, 7306_4, 7310_2, 7324_3, 7327_3, 7330_3, 7333_3, 7334_3, 7337_3, 7365_3, 7366_4, 7370_3, 7392_4, 7393_4, 7422_3, 7907_3	∀	∀	∀

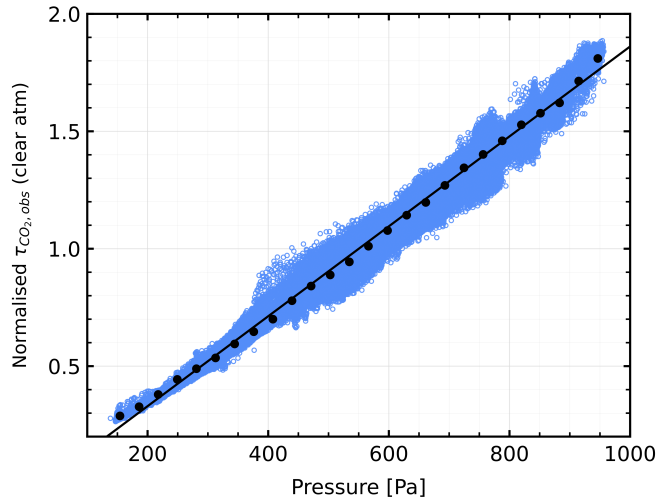


Figure 4: Calibration of $\tau_{CO_2, pred}$ pressure dependency (equation 6). This graph represents the observed CO₂ optical depths of 57 OMEGA observations (blue circles) as a function of pressure. CO₂ optical depths are normalised to take into account albedo and incidence variations previously determined in Figures 2 and 3. Median values are computed on pressure ranges of 32 Pa width (black circles) to better constrain the linear fit (solid black line; see Table 3 for parameter values).

constant (variations respectively less than 10 Pa and less than 0.10, see Table 2 and Figure 3 for more details). The behaviour of the observed CO₂ optical depth as a function of incidence is shown in Figure 3. We observe that variations are small (about 7%) for low-medium incidences ($i < 40^\circ$)

and large (about 40%) for high incidences ($i > 60^\circ$). These observations lead to an exponent $d \simeq 0.53$.

Finally, we use 57 observations (see Table 2) to constrain the parameter α which characterises variations with pressure (Figure 4). This last calibration step is done without any restrictions on these observations (albedo nor incidence) as we account for albedo and incidence variations using $f(Alb)$ and d described above. Pressure is evaluated using the pressure calculator (pres0) of the Mars Climate Database (MCD, version 4.1) (Forget et al., 1998; Millour et al., 2018), which takes OMEGA pixel information (latitude, longitude, altitude, solar longitude and local time) as inputs. The main hypothesis of the calculator is to consider the total pressure at the surface equivalent to the hydrostatic pressure (the weight of the column of atmosphere above the surface), which is true in the great majority of Martian meteorological conditions. It is also connected to the simulation outputs of the Mars Planetary Climate Model of the *Laboratoire de Météorologie Dynamique* (LMD). Therefore, it takes into account the seasonal variations of the pressure that are linked to the CO₂ cycle (Forget et al., 1998). As expected, we observe in Figure 4 an increasing linear trend between $\tau_{CO_2, pred}$ and pressure. Note however that the intercept is not exactly null.

Overall, we thus obtain equation 8: associated parameters are summarised in Table 3.

$$\tau_{CO_2, pred} = \alpha P \left(1 + \left(\frac{1}{\cos(i)} \right)^d \right) \times \frac{A_{max}}{1 + \left(\frac{A_{max}}{A_0} - 1 \right) e^{-k \times Alb}} + b \quad (8)$$

Table 3

Parameters values for equations 6, 7 and 8.

Parameters	Values
α	7.39×10^{-4}
d	5.29×10^{-1}
A_{max}	1.03
A_0	8.44×10^{-1}
k	1.26×10^1
b	-2.39×10^{-2}

3.4. Dust optical depth calibration using Mars Exploration Rovers

In this section, we describe how $\Delta\tau_{CO_2}$ (equation 1) relates to the dust optical depth (τ_{dust}) using observations gathered in the vicinity of Mars Exploration Rovers (MER hereinafter). These two rovers, Spirit and Opportunity, have operated respectively on Gusev crater and Meridiani Planum, during the same period as OMEGA, between January 2004 and March 2010 (MY 26-29) for Spirit, between January 2004 and February 2019 for Opportunity (MY 26-34). Atmospheric extinction optical depth has been computed in Lemmon et al. (2015) by using the Pancam solar images (0.88 μ m) of the two rovers, allowing an accurate characterisation of the annual and interannual dust variability from the Martian surface. We consider that these MER measurements of optical depth (τ_{MER}) are a "ground truth" reference for our calibration procedure. Note that Lemmon et al. (2015) suggest to use these 0.88 μ m measurements to compare them to other datasets.

To carry out the correspondence between $\Delta\tau_{CO_2}$ and τ_{MER} , we used 38 OMEGA observations near MER landing sites. Two areas of interest have been defined: [173, 177] $^{\circ}$ E and [12, 17] $^{\circ}$ S for Spirit, [353.5, 355.5] $^{\circ}$ E and [1.7, 2.7] $^{\circ}$ S for Opportunity. Within these areas we use only OMEGA pixels with altitudes in the [-2, -1.9] km range for Spirit and [-1.58, -1.38] km for Opportunity (values close to the rover location altitudes). Note that we apply different spectral filters on OMEGA observations (see section 2.2) to exclude, among other things, ice clouds (main aerosols with dust) that can change the atmospheric extinction optical depth. So, it is assumed that for OMEGA/MER co-observations the MER measurements are equivalent to dust extinction optical depths.

The quantity that we compare to τ_{MER} is $\Delta\tau_{CO_2}/\tau_{CO_2, pred}$, which is $\Delta\tau_{CO_2}$ normalised by the clear atmosphere CO_2 optical depth. Therefore, our dust index is normalised in pressure. As a consequence, we will compare this index to τ_{MER} normalised to a constant reference pressure (610 Pa).

We first evaluate the relation between $\Delta\tau_{CO_2}/\tau_{CO_2, pred}$ and τ_{MER} for low to moderate incidence angles ($\leq 50^{\circ}$) in Figure 5. We observe an overall increasing linear trend between both quantities (equation 9), with some dispersion at low optical depths. We also notice that the slope $\gamma(Alb)$ depends on surface albedo.

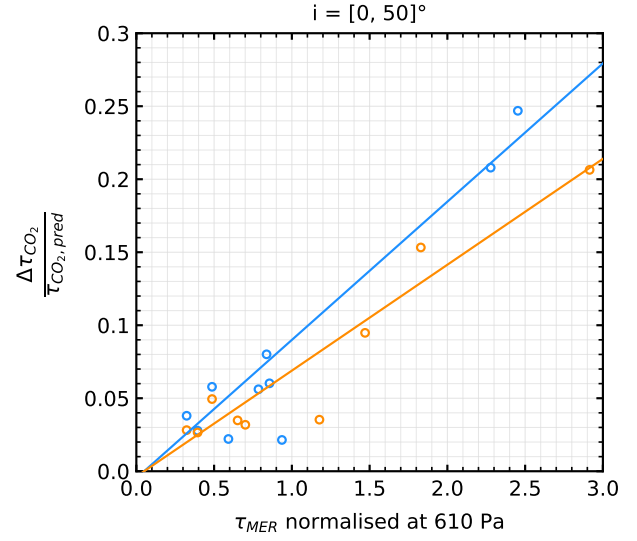


Figure 5: Relation between $\Delta\tau_{CO_2}/\tau_{CO_2, pred}$ and τ_{MER} for OMEGA observations with $i \leq 50^{\circ}$. This graph represents observation median values of $\Delta\tau_{CO_2}/\tau_{CO_2, pred}$ for two albedo ranges [0.255, 0.265] (blue points) and [0.395, 0.405] (orange points) as a function of τ_{MER} normalised at 610 Pa. A linear fit has been realised for each albedo range (blue and orange solid lines).

$$\frac{\Delta\tau_{CO_2}}{\tau_{CO_2, pred}} = \gamma(Alb) (\tau_{MER} - 0.05) \quad (9)$$

We evaluate empirically $\gamma(Alb)$ using data in Figure 6 (see legend for details). The fit parameters of resulting equation 10 are provided in Table 4.

$$\gamma(Alb) = \begin{cases} B Alb + C & \forall Alb \leq Alb_{cut} \\ D e^{\kappa(Alb - Alb_{cut})} + E & \forall Alb \geq Alb_{cut} \end{cases} \quad (10)$$

At high incidence angles, most photons are scattered by atmospheric dust, which means that the CO_2 optical path is more sensitive to the presence of dust. Consequently, the relation between $\Delta\tau_{CO_2}/\tau_{CO_2, pred}$ and τ_{MER} is modified for incidences greater than 50° . We evaluate this in Figure 7 where we show that for a given τ_{MER} , $\Delta\tau_{CO_2}/\tau_{CO_2, pred}$ increases according to the function defined in equation 11 ($i \geq 50^{\circ}$) where the exponent β depends linearly on τ_{MER} (see Figure 8, equation 12 and Table 4).

$$\frac{\Delta\tau_{CO_2}}{\tau_{CO_2, pred}} = \gamma(Alb) (\tau_{MER} - 0.05) \frac{1 + \left(\frac{1}{\cos i}\right)^{\beta(\tau_{MER})}}{1 + \left(\frac{1}{\cos 50^{\circ}}\right)^{\beta(\tau_{MER})}} \quad (11)$$

$$\beta(\tau_{MER}) = m \tau_{MER} + q \quad (12)$$

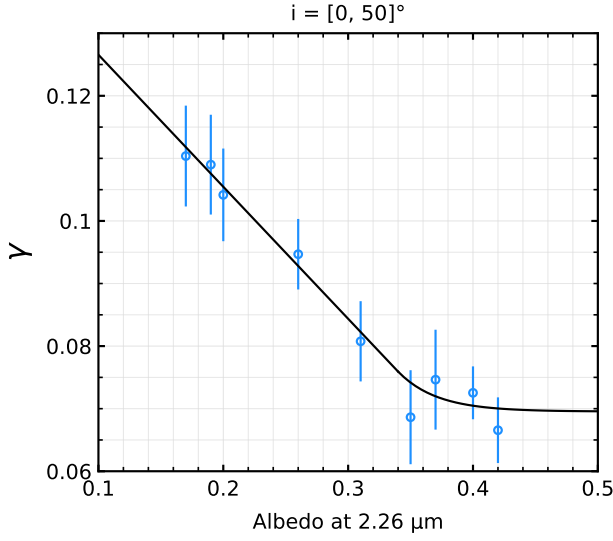


Figure 6: Calibration of the $\gamma(\text{Alb})$ albedo dependence of $\Delta\tau_{\text{CO}_2}/\tau_{\text{CO}_2, \text{pred}}$ (equation 9). The slope of several fits similar to the two examples provided in Figure 5 is shown as a function of albedo. The derived empirical function is detailed in equation 10 and Table 4.

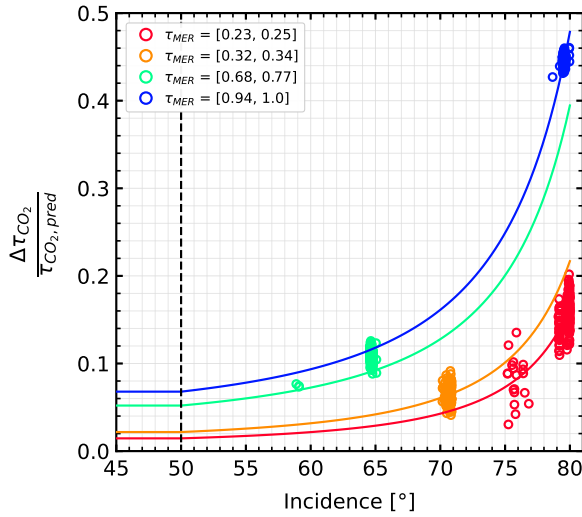


Figure 7: $\Delta\tau_{\text{CO}_2}/\tau_{\text{CO}_2, \text{pred}}$ as a function of incidence angles ($i > 45^\circ$) are shown for four different τ_{MER} ranges (colors). Albedos between 0.33 and 0.34 are only used. For $i < 50^\circ$ (symbolised by the vertical dashed line), the y-axis values are provided by equation 9. For $i > 50^\circ$, we fit equation 11 (solid lines) on available data points (circles). Each fit differs by the exponent $\beta(\tau_{\text{MER}})$ value.

Overall, we thus link $\Delta\tau_{\text{CO}_2}/\tau_{\text{CO}_2, \text{pred}}$ and τ_{MER} through two equations: equation 9 for $i \leq 50^\circ$ and equation 11 for $i \geq 50^\circ$.

This calibration procedure makes it possible to convert a $\Delta\tau_{\text{CO}_2}/\tau_{\text{CO}_2, \text{pred}}$ calculated with OMEGA data into an OMEGA dust optical depth τ_{dust} using a lookup table. This lookup table is populated by the previous equations, in

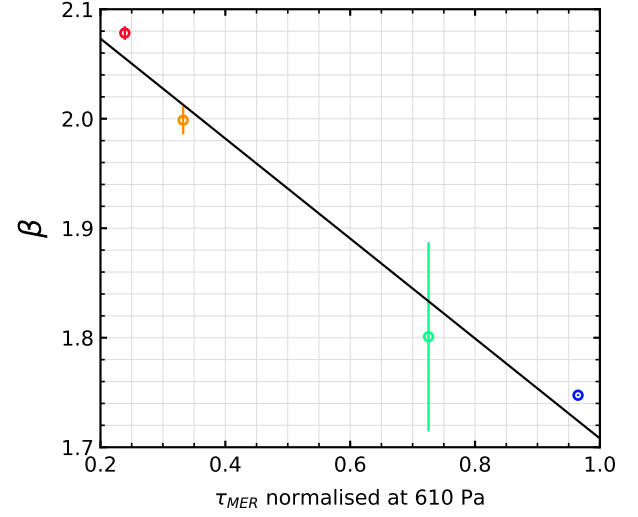


Figure 8: Calibration of $\beta(\tau_{\text{MER}})$ (equation 11). Each point is extracted from Figure 7 and used to constrain $\beta(\tau_{\text{MER}})$ function (black solid line, equation 12).

Table 4

Parameters values for equations 9, 10, 11, and 12.

Parameters	Values
B	-2.11×10^{-1}
C	1.48×10^{-1}
$D = B \text{ Alb}_{\text{cut}} + C - E$	6.38×10^{-3}
E	6.95×10^{-2}
κ	3.21×10^1
Alb_{cut}	0.34
m	-4.56×10^{-1}
q	2.16

which " τ_{MER} " now corresponds to " τ_{dust} ". We illustrate the overall consistency of this approach by comparing τ_{dust} to τ_{MER} in Figure 9 for all available OMEGA/MER co-observations. We can notice that the point dispersion (from the $y = x$ line) does not depend on the dust optical depth. So, we compute the global standard deviation of the difference between τ_{MER} and τ_{dust} : 0.2, which can be used as an uncertainty for τ_{dust} as represented in Figure 9 as error bars. In the next section, we apply this calculation to the entire OMEGA dataset to derive NIR ($0.9 \mu\text{m}$) τ_{dust} and monitor atmospheric dust on Mars.

4. Results and discussions

4.1. Global seasonal maps

We constructed global seasonal maps of dust optical depth using this OMEGA dataset. Each Martian year among MY 27, 28, and 29 is divided into six ranges of solar longitude 60° wide (see Figures 10, 11 and 12). Two additional maps for late MY 26 and early MY 30 (beginning of Mars Express operations and end of the OMEGA C-channel respectively) were also constructed (Figure 13). We use the

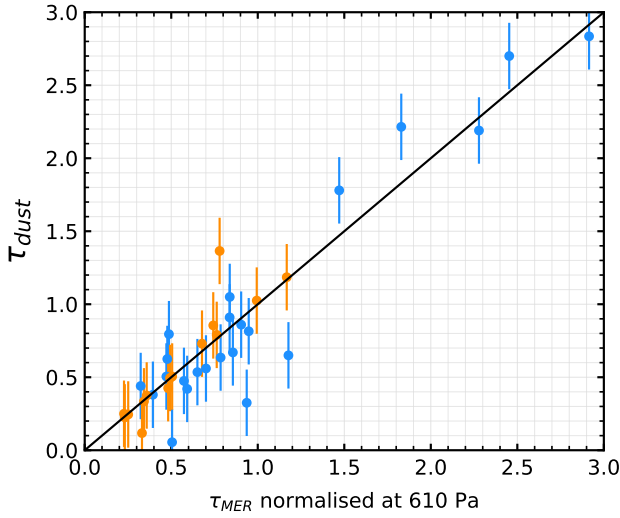


Figure 9: Consistency of the MER calibration. This graph represents the median value of τ_{dust} for all OMEGA observations used for this calibration as a function of τ_{MER} . Observations with a low-medium incidence angles ($\leq 50^\circ$) are symbolised by blue circles and those for higher angles by orange circles. The error bars represent the standard deviation between τ_{MER} and τ_{dust} . The $y = x$ line is represented by a solid black line.

HEALPix pixelisation of the Martian sphere with an average spatial sampling of 5° in latitude and 6° in longitude, and we use a Mollweide projection (accuracy of proportions in area) to represent the maps. Each OMEGA observation cross several map pixels and a given map pixel can be covered by several OMEGA observations in a given solar longitude range. Consequently, the filling method of these maps is as follows: for each OMEGA observation and for a given map pixel, we compute the τ_{dust} median value of the OMEGA pixels located within the map pixel. If there are different OMEGA observations passing through the same map pixel, the maximum value between the median values of these observations is selected, so as to emphasis dust storm events (selecting the mean instead of the maximum only marginally changes these maps).

At global scale and first order, we observe the well-known seasonality of Martian dust: the global level of τ_{dust} is higher during the dust season ($L_s = 180 - 300^\circ$) than in the clear atmosphere period ($L_s = 0 - 120^\circ$). At second order, we can see that the spatial distribution of atmospheric dust is not homogeneous regardless of the season: localised higher values are observed in all maps, even during the clear season, such as in MY 29 at $L_s = 0 - 60^\circ$ (top left panel of Figure 12) around 315°E and 20°S near Valles Marineris, where a dust storm is indeed present in the corresponding OMEGA observation.

We observe that some Martian areas have more atmospheric dust activity than others. For example, the Hellas basin ($40 - 100^\circ\text{E}$, $20 - 60^\circ\text{S}$), a well-known dust source and sink (Cantor et al., 2001; Szwest et al., 2006), has high dust optical depths over most of the year. As discussed in

the previous section, our procedure aims at estimating a dust optical depth normalised to a constant pressure level. Hence, these high values of optical depth over Hellas do correspond to a specific local increased in normalised opacity. Actually, we do not observe any systematic correlation between our (pressure normalised) dust optical depth and altitude. We can for example observe in Figure 12 that optical depth can be high over Hellas while being simultaneously low in some other low altitude areas (e.g., northern plains at $L_s = 0 - 60^\circ$). We can also note that there is no optical depth decrease over high altitude areas in these maps, such as Tharsis ($\sim 245^\circ\text{E}$, $\sim 0^\circ\text{N}$), as could be seen if the dust optical depth was correlated with altitude.

These maps also highlight some major routes taken by dust storms according to previous studies, mainly from the northern hemisphere to the southern one (Battalio and Wang, 2021; Wang and Richardson, 2015, see respectively their Figures 8 and 6). Medium to high values of dust optical depth are indeed observed over these routes, such as for the Acidalia-Chryse ($\sim 325^\circ\text{E}$) channel, or Arcadia-Cimmeria/Sirenum ($\sim 180^\circ\text{E}$) route (e.g., see MY 29 $L_s = 300 - 360^\circ$ map in Figure 12).

The OMEGA dataset covers the MY 28 GDS that occurred between $L_s \sim 265^\circ$ and 310° (Figure 11) which is detailed in two sub-maps in Figure 14. We observe high dust optical depths from Chryse to Noachis ($\sim 345^\circ\text{E}$) just before the beginning of the GDS in the $L_s = 240 - 265^\circ$ range (more precisely at $L_s = 264.4^\circ$). This area corresponds to two dust storms also reported in Wang and Richardson (2015) before the GDS onset. GDS initiation probably occurred slightly later at the east of Hellas ($\sim 50^\circ\text{E}$) according to Wang and Richardson (2015), where and when we also observe high dust optical depths in an OMEGA observation obtained at $L_s = 264.9^\circ$ (Figure 14, top panel).

4.2. Comparison with previous thermal IR studies

From the OMEGA dataset we can also produce latitude/solar longitude diagrams of dust optical depth for MY 26, 27, 28, 29 and 30 (see Figure 15). At first order, observed relative variations with season and latitude are in good agreement with those derived from Thermal-Infrared (TIR hereinafter) data (Montabone et al., 2015, see their Figure 16). At second order, we can notice a few differences. For example, $L_s = 305 - 335^\circ$ storms (named "C-storms" in Kass et al. (2016)) have lower values of optical depth compared to $L_s = 240 - 300^\circ$ storms in TIR retrievals (Montabone et al., 2015), while both periods have similar NIR optical depth levels (see Figure 15).

These differences can be studied by computing the NIR/TIR dust optical depth ratio. Such variations of this ratio have implications for general circulation models, as these models rely on radiative budget calculations in both the solar and the TIR range (Forget et al., 1999). Hence, the knowledge of the dust optical depth NIR/TIR ratio is required, in addition to the amount of dust, to perform accurate predictions. So, we have calculated the ratio between our dust extinction optical depth values derived in

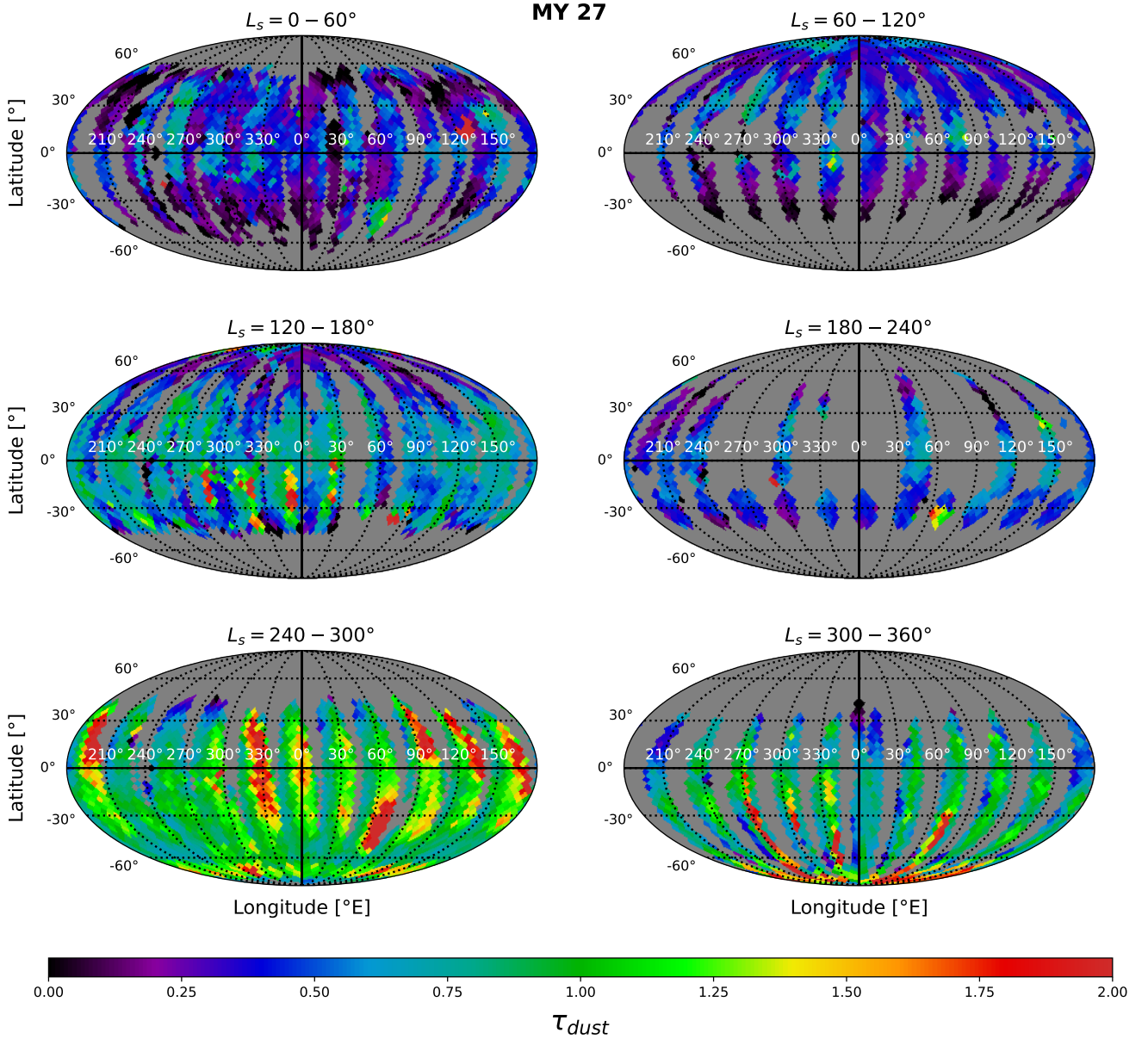


Figure 10: Seasonal maps of dust optical depth computed with OMEGA data for MY 27. Each map corresponds to a range of 60° of solar longitude. A Mollweide projection is used. See section 4.1 for details. On the color bar, the black corresponds to $\tau_{dust} = 0$ and the darkest red corresponds to $\tau_{dust} \geq 2$.

NIR (OMEGA) and TIR $9 \mu\text{m}$ extinction Column Dust Optical Depth (CDOD) normalised at 610 Pa provided by Montabone et al. (2015) on the basis of contemporary TES/MGS, THEMIS/MO and MCS/MRO data (see their Figure 1). The resulting histogram is shown in Figure 16. The ratio distribution peaks at 1.8, which is in agreement with the values (between 1.25 and 5) computed locally with MER data in Lemmon et al. (2015) using Pancam in NIR and Mini-TES in TIR (see their Figure 10). This average ratio is also consistent with Montabone et al. (2015) who consider a 2.6 value for the NIR extinction to TIR absorption ratio. Indeed, this corresponds to an extinction/extinction

ratio of 2 using a 1.3 conversion factor between absorption and extinction at $9.3 \mu\text{m}$ (Wolff et al., 2006). We can notice that the distribution is very large with a 1.5 "equivalent standard deviation" (defined by the half difference of the boundaries of the interval that contains 68% of the values). Knowing that the NIR/TIR ratio depends on the dust particle size (Wolff et al., 2006, see their Figure 13), we compare our distribution with expected variations caused by particle size in Figure 16. Size variations as a function of place and season probably explain part of the distribution width, apart from very high or very low ratio values. These latter could correspond to specific events observed by one of the two

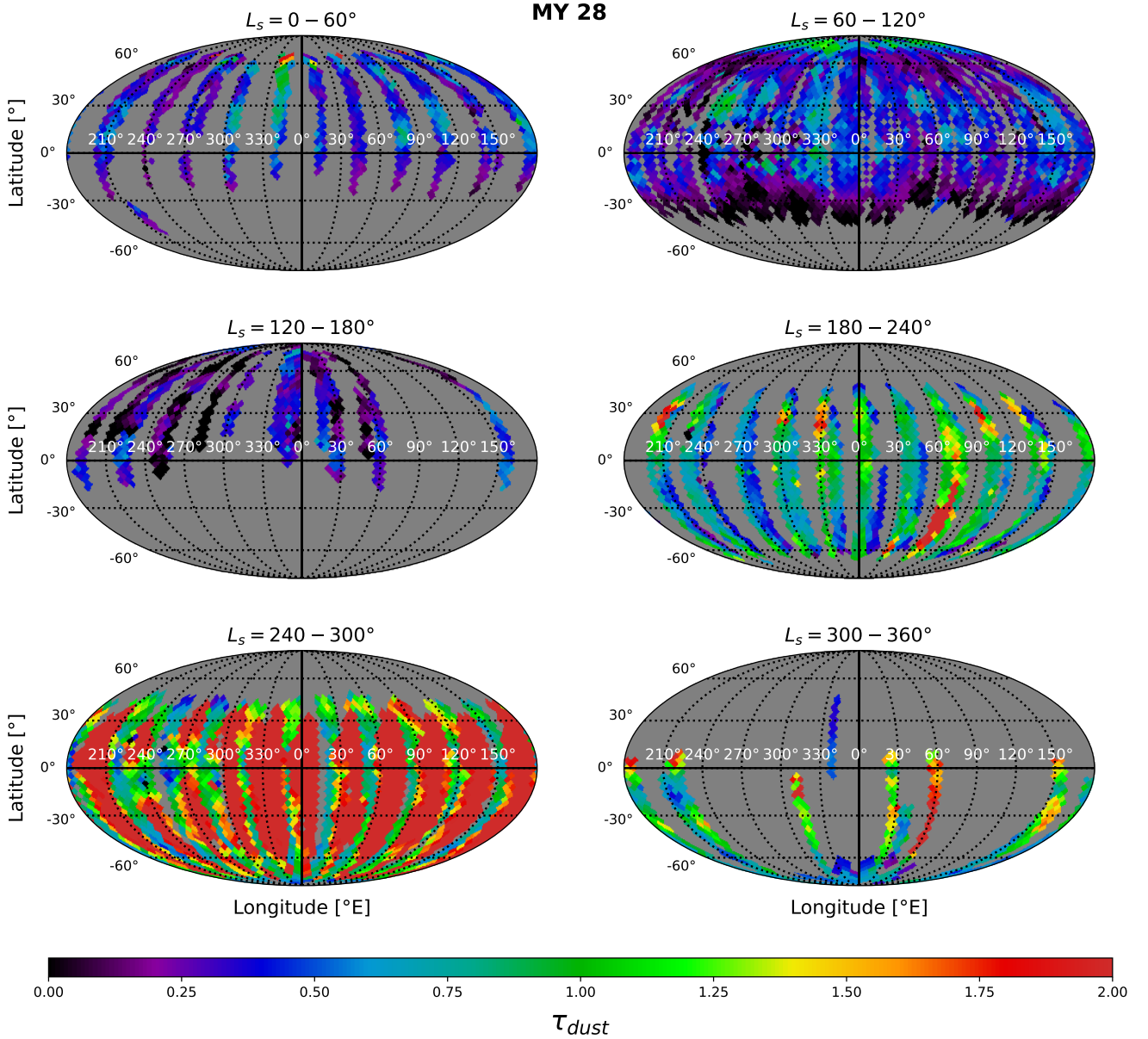


Figure 11: Seasonal maps of dust optical depth computed with OMEGA data for MY 28. Each map corresponds to a range of 60° of solar longitude. A Mollweide projection is used. See section 4.1 for details. On the color bar, the black corresponds to $\tau_{dust} = 0$ and the darkest red corresponds to $\tau_{dust} \geq 2$.

instruments only, or this may result from retrieval biases. Actually, biases specific to each method have already been identified. For example, the impact of a given amount of atmospheric dust on the CO_2 optical depth will depend on dust vertical distribution (e.g., well-mixed or not), while we do not include this level of refinement in our modelling.

4.3. Particle size variations during the MY 28 GDS

We used results presented in Figure 13 of Wolff et al. (2006) to convert the dust extinction optical depth NIR/TIR ratio to r_{eff} (considering an effective variance of 0.3). We restrict this conversion to OMEGA $\tau_{dust} = [0.5, 2.5]$ and

NIR/TIR ratio values between 1 and 4. We show two examples of particle size variations observed with this method during the 2007/MY 28 GDS in Figures 17 and 18.

During the peak of the GDS (maximum latitudinal extension, $L_s = [271, 275]^\circ$), we observe that particle size decreases with latitude from the equator towards the south pole, while optical depth is high and nearly constant with latitude (Figure 17). Latitudinal variations of r_{eff} have already been observed in Wolff and Clancy (2003) for the 2001A GDS (see their Figures 15 and 16). This observation could be explained by the greater ability of small particles to

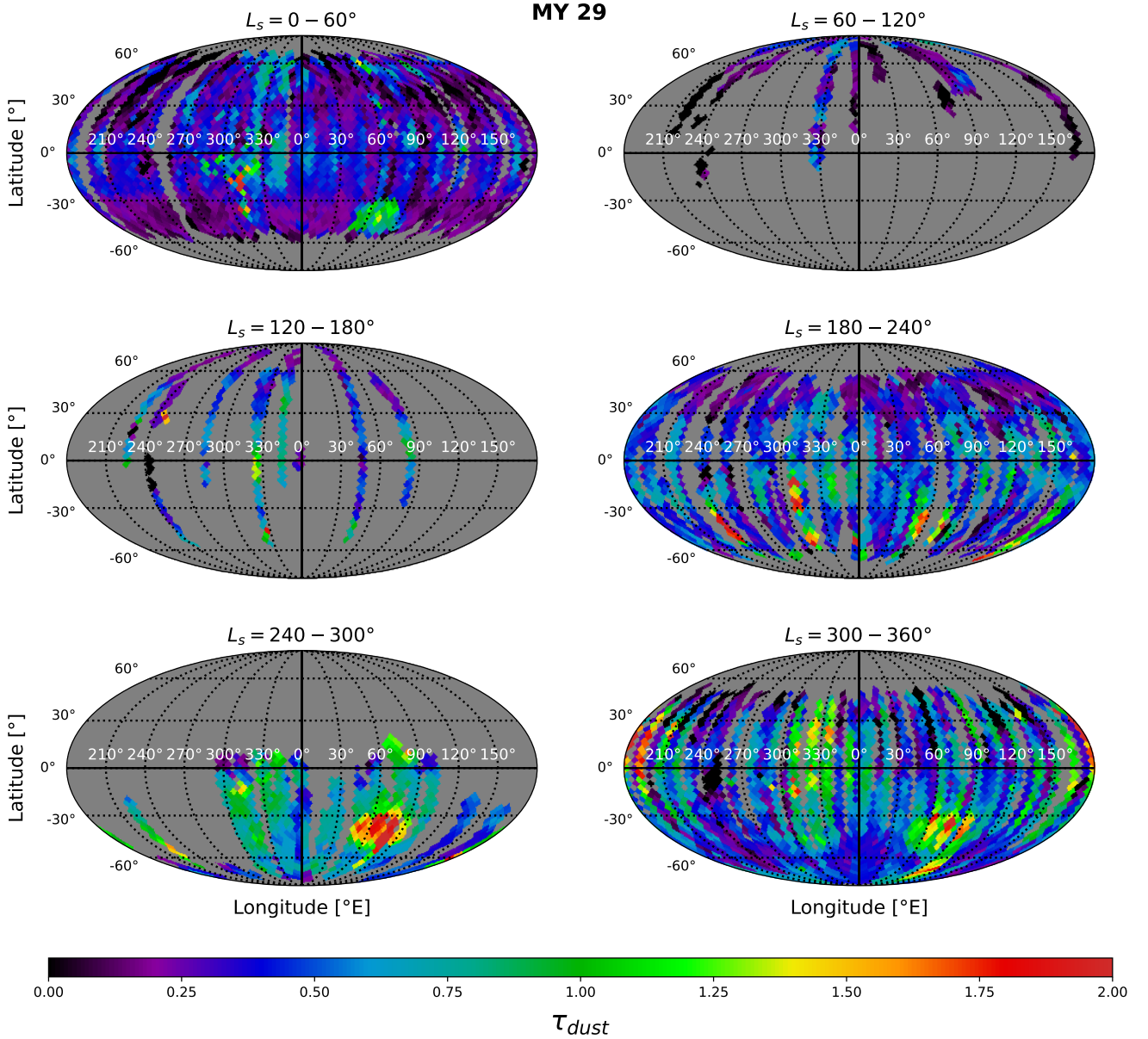


Figure 12: Seasonal maps of dust optical depth computed with OMEGA data for MY 29. Each map corresponds to a range of 60° of solar longitude. A Mollweide projection is used. See section 4.1 for details. On the color bar, the black corresponds to $\tau_{dust} = 0$ and the darkest red corresponds to $\tau_{dust} \geq 2$.

be transported (e.g., by the Hadley cell circulation) far from the GDS initiation area.

We also note an overall increase and then decrease of the particle size that correlates in time respectively with the onset and decay of the 2007 GDS (Figure 18). Such an increase in the effective dust particle size is expected during dust storms, due to convective movements and vertical mixing overcoming gravitational sedimentation of dust particles (e.g., Haberle et al. (1982), Kahre et al. (2008), Spiga et al. (2013)) and dust coagulation processes (Bertrand et al., 2022). For instance, the modelling of the 2018 GDS revealed strong updrafts associated with plumes of dust and

an increase in particle size (Bertrand et al., 2020), which was confirmed by observations ("dust towers", Heavens et al. (2019)). The median value of the effective radius varies from $1.1 \mu\text{m}$ before/after the GDS to $1.5 \mu\text{m}$ during the GDS. This average trend is in agreement with retrievals reported during the same GDS with another method by Vincendon et al. (2009) (see their Figure 15). Note that maximum values reach $2.3 \mu\text{m}$ (Figure 18), which is the maximum possible value of our retrieval method (see Figure 13 of Wolff et al. (2006)). The existence of higher values up to $3\text{--}4 \mu\text{m}$ reported for other GDS (Wolff and Clancy, 2003; Lemmon et al., 2019) is not evaluated here.

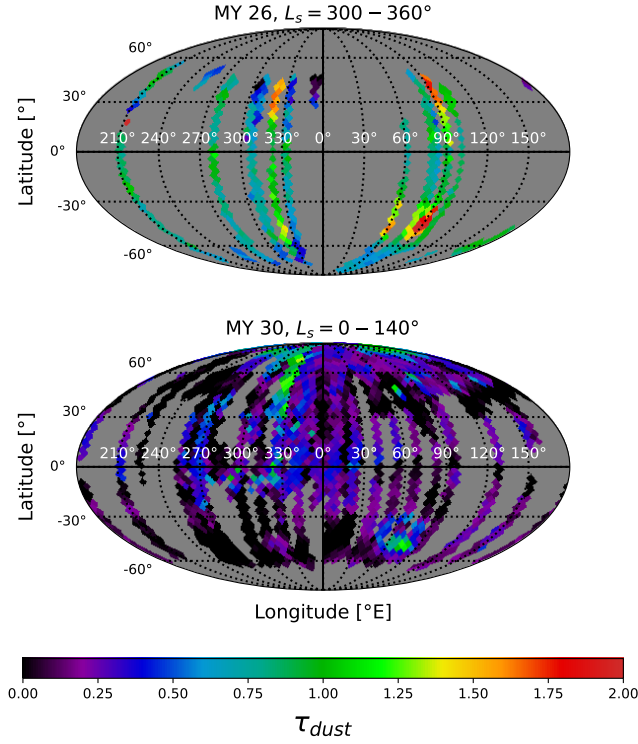


Figure 13: Two additional maps of dust optical depth obtained during late MY 26 (top) and early MY 30 (bottom). MY 26 map starts from the arrival of Mars Express and MY 30 map goes up to the breakdown of OMEGA C-channel. These maps and the color bar are produced similarly as those presented in Figures 10, 11 and 12.

4.4. Search for MY 28 GDS precursory signs

We can notice that our τ_{dust} map obtained in MY 27 in the $L_s = 240 - 300^\circ$ range (storm season) (Figure 10) is similar to the one obtained by MGS/TES in MY 24 in the same L_s range (Wang and Richardson, 2015, see their Figure 8). As both MY 27 and 24 are years that precede a GDS (2007 and 2001 respectively), we have looked for differences between the year before and after the 2007 GDS, so as to see if the year preceding the storm shows precursory signs.

The different spatial coverage of our global maps and the large time range of these maps can introduce some biases. Hence, it is necessary to use both global maps (Figures 10, 11, 12, and 13) and latitude/ L_s diagrams (Figure 15) to extract trends. We observed that MY 27 (before the GDS) and MY 29 (after the GDS) are comparable in term of dust optical depth at a year scale, with few differences such as a regional dust storm in MY 27. This is in agreement with local MER measurements from the surface (Lemmon et al., 2015, see their Figure 7) and global TIR measurements from the orbit (Montabone et al., 2015, see their Figure 16). Thus, we do not observe obvious significant distinctive signs the year before the MY 28 GDS.

The combination of these three datasets however suggests some differences not the year, but the season preceding the GDS. If we compare this pre-GDS season (from $L_s \sim$

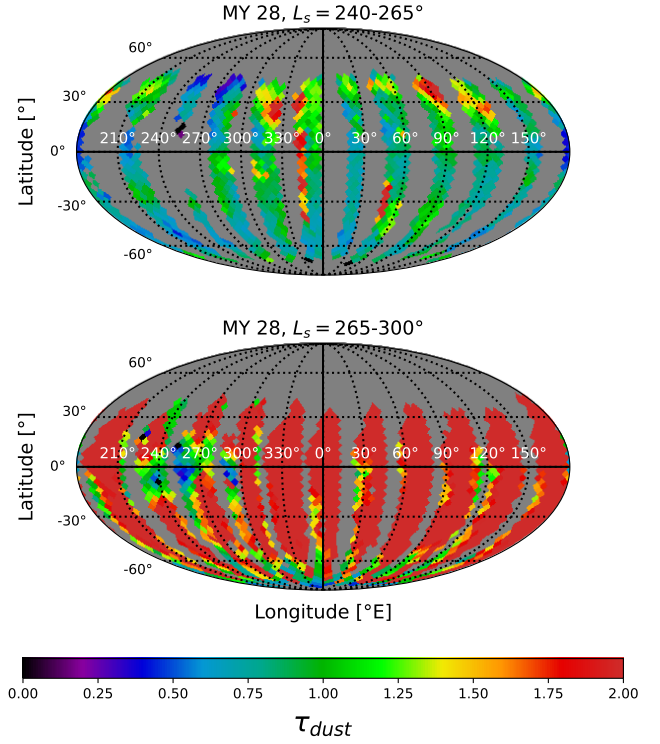


Figure 14: Two sub-maps of dust optical depth derived from MY 28 $L_s = 240 - 300^\circ$ map (bottom left panel of Figure 11). On top: $L_s = 240 - 265^\circ$ period that precedes the GDS, and on bottom: $L_s = 265 - 300^\circ$ period during the GDS. These maps and the color bar are produced similarly as those presented in Figures 10, 11 and 12.

150° to 260°) between MY 27, 28 and 29, we observe lower optical depths in MY 28, in particular between $L_s \sim 240^\circ$ and 260° , as previously noticed in Meridiani by Lemmon et al. (2015). The 2007 GDS is a late GDS contrary to the 2001 and 2018 one: such lower activity in the early storm season could thus be a precursory sign of a late storm season GDS.

4.5. Link with RSL

Recurring Slope Lineae (hereinafter RSL) may form when and where unstable dust has been recently deposited on the surface, and when and where winds are strong enough to remove dust or initiate dust removal on a slope (Vincendon et al., 2019). In the northern hemisphere, we can see in the panel A of Figure 19 that confirmed RSL (red markers) have been predominantly reported near Chryse-Acidalia Planitia (Stillman et al., 2016; Stillman, 2018). These RSL take place inside the Acidalia-Chryse dust storm travel route discussed previously (see section 4.1), which is also a low albedo area (like most RSL sites, McEwen et al. (2011)). These two characteristics (low albedo and high atmospheric dust activity) show that Chryse-Acidalia is an area where winds are strong enough to remove dust from the surface (Thomas et al., 2003), and to initiate dust storms or to transport atmospheric dust. Additionally, we observe that this RSL area has higher dust optical depth values than its surrounding

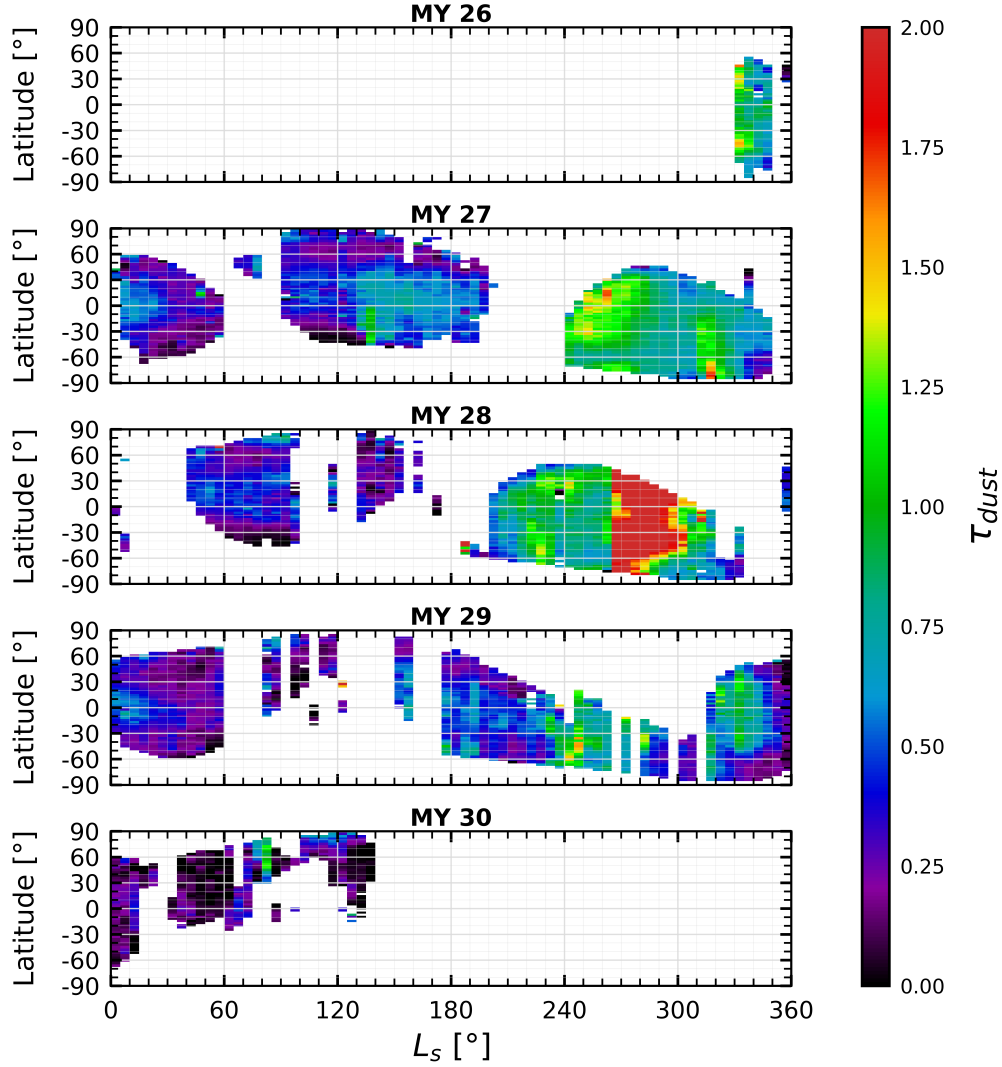


Figure 15: Overview of atmospheric dust distribution for the three full Martian years (MY 27, 28, 29) and the two partial years corresponding to the beginning (MY 26) and the ending (MY 30) of OMEGA C-channel operations. Zonal means of dust optical depth maps as a function of latitude and season (L_s) are shown. For each solar longitude range of 5° , we computed the average of τ_{dust} for all longitudes and for latitude bin about 3.2° width.

during two periods of major RSL formation (i.e., when dust is expected to be removed from the surface): $L_s = 300 - 360^\circ$ and $L_s = 0 - 60^\circ$ (see respectively panels B and C of Figure 19). Actually, at mid-latitudes, the longitudes of Chryse-Acidalia RSL are the only ones that correspond to a local maximum of atmospheric dust optical depth for both $L_s = 300-360^\circ$ and $L_s = 0-60^\circ$ (see panel D of Figure 19). Thus, these northern hemisphere RSL are correlated with atmospheric dust in time and space.

5. Summary and conclusions

- We have developed and applied a new method to detect atmospheric dust in the Mars Express/OMEGA Near-Infrared (NIR) dataset. Atmospheric dust reduces the strength of the $2\ \mu\text{m}$ CO_2 gas absorption

band: comparing the observed bands with model predictions for clear atmosphere makes it possible to detect atmospheric dust.

- We then analysed co-observations from the orbit by OMEGA and from the surface by the Mars Exploration Rovers to calibrate OMEGA dust detections and to convert our measurements at $2\ \mu\text{m}$ to $0.9\ \mu\text{m}$ "NIR" dust optical depths.
- We applied this method to the OMEGA dataset to derive seasonal global maps of dust optical depth from late MY 26 to mid MY 30 (Figure 10, 11, 12 and 13). Main well-known features of the dust cycle, such as dust storm travel routes (Acidalia-Chryse $\sim 325^\circ\text{E}$, Arcadia-Cimmeria/Sirenum $\sim 180^\circ\text{E}$) or major dust sources/sinks (e.g., Hellas) are recognisable.

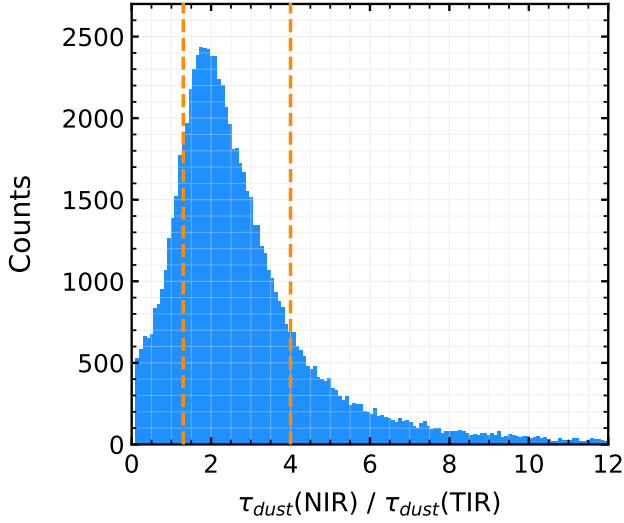


Figure 16: Histogram of the dust extinction optical depth ratio between NIR (OMEGA, this study) and TIR (Montabone et al., 2015). The distribution peaks at 1.8. The vertical dashed orange lines represent ratio values 4 and 1.35 that correspond to dust particle size $r_{eff} = 0.7$ and 2.1 respectively (for an effective variance of 0.3) according to Wolff et al. (2006).

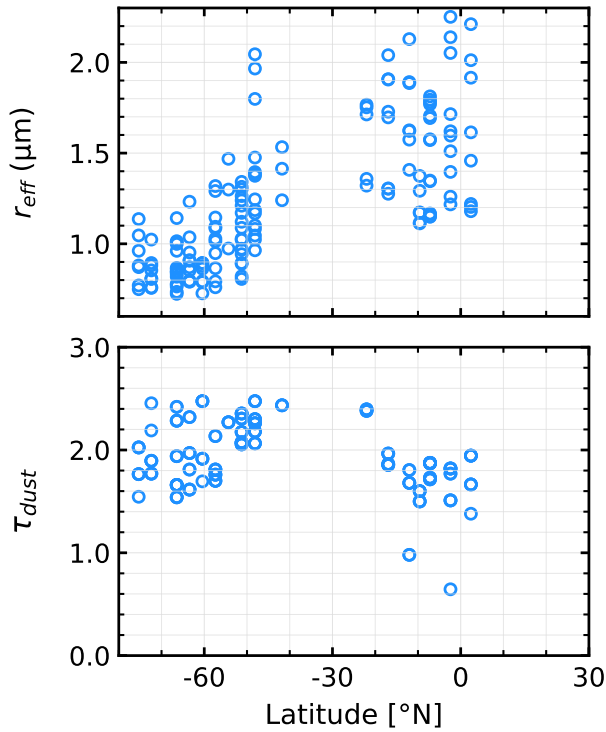


Figure 17: Variations with latitude of (top) dust effective radius and (bottom) dust optical depth during MY 28 for $L_s = [271, 275]^\circ$. All longitudes are considered (see section 4.2 for details).

- We did not identify major significant differences between the year preceding and the year following the Global Dust Storm (GDS). However, we note that the

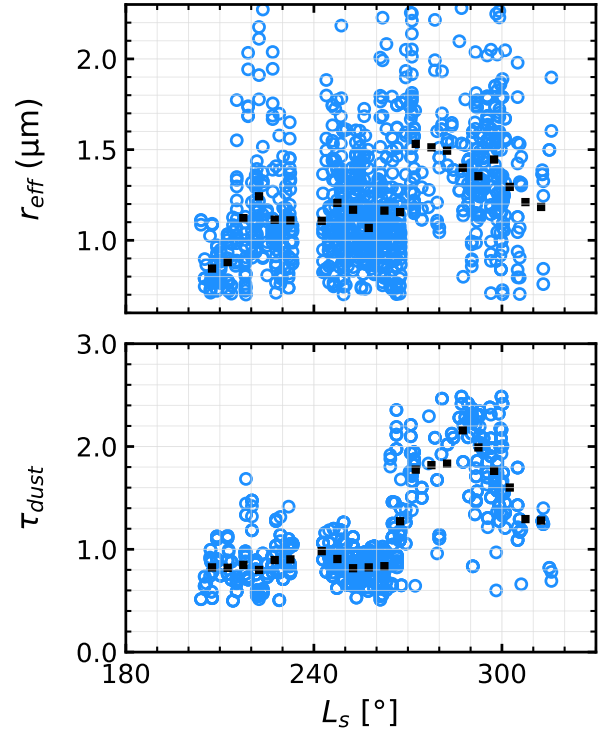


Figure 18: Variations with solar longitude of (top) dust effective radius and (bottom) dust optical depth during MY 28. Longitudes in the $[-10, 10]^\circ N$ range are considered (each blue circle corresponds to a map pixel). Black squares represent the mean values for $5^\circ L_s$ range width (see section 4.2 for details).

beginning of the dust season prior to the onset of the MY 28 GDS was less intense in MY 28 compare to the same period of MY 27 and MY 29.

- We compared our NIR ($0.9 \mu m$) dust optical depth with TIR ($9 \mu m$) values derived in previous studies: the NIR/TIR extinction optical depth ratio is 1.8 on average (Figure 16) which is in agreement with previous results.
- We have converted this optical depth ratio to particle size. We observed latitudinal and seasonal variations of dust mean particle size linked to the MY 28 GDS.
- We observed that Recurring Slope Lineae (RSL) location and timing in the northern hemisphere correlate with atmospheric dust activity (Figure 19). This correlation suggests that the RSL activity is linked to surface dust rising and/or atmospheric transport phenomena.
- Finally, we can notice that this method could be adapted to other orbital NIR imaging spectrometer datasets such as CRISM/MRO or MIRS/MMX.

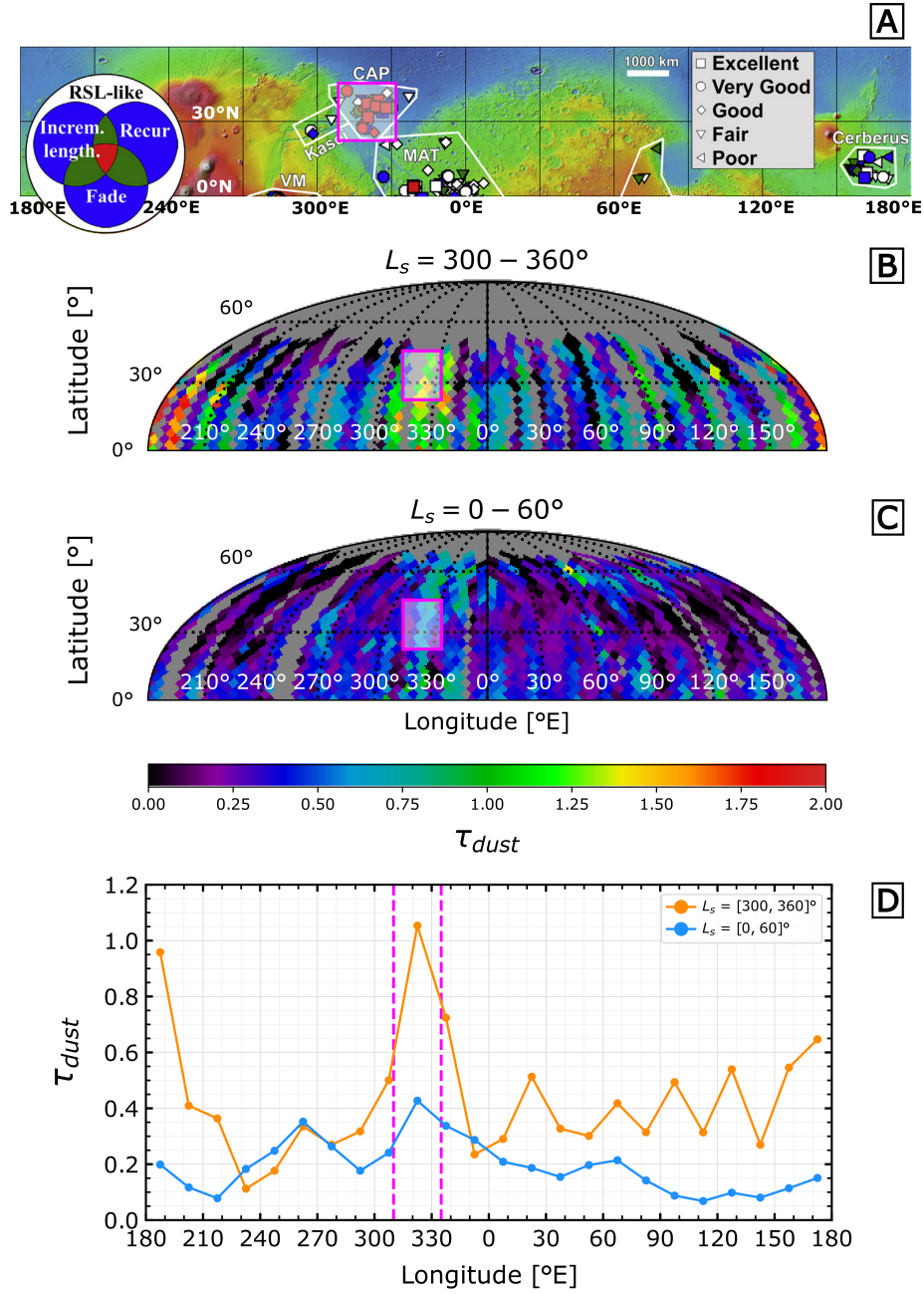


Figure 19: Illustration of the time and spatial correlation between atmospheric dust and RSL in the northern hemisphere. [A] is a modified version of Figure 2.1 of Stillman (2018) which represents the distribution of RSL in different sites on a topographic map (here for the northern hemisphere), with a specific legend (color and shape) to characterize the RSL detections. [B] and [C] are MY 29 seasonal global maps (northern hemisphere) of dust optical depth. The pink rectangle corresponds to the main area of confirmed RSL (red symbols) in the northern hemisphere from panel [A]. [D] longitudinal profile of dust optical depth from [B] (orange) and [C] (blue) maps, for a $25^\circ - 45^\circ$ N latitude ring that includes most northern hemisphere confirmed RSL (pink rectangle). The longitudes of RSL are indicated with pink dotted lines.

Acknowledgments

The OMEGA/Mex data are freely available on the ESA PSA at <https://archives.esac.esa.int/psa/#!Table%20View/OMEGA=instrument>.

The authors thank the reviewers for their pertinent and helpful comments that really improve the quality of this paper. The first author also wants to thank A. Stcherbinine

for having developed such a useful Python tool (OMEGA-Py).

The authors have a thought for Brigitte Gondet who passed away this year and who was an important member of the Mars Express mission, working among other things to improve the OMEGA dataset from the beginning of the

mission until now. Her person and expertise will be missed.
Merci Brigitte!

References

- Antoniadi, E.M., 1930. La Planete Mars. Etude basee sur les resultats obtenus avec la grande lunette de l'Observatoire de Meudon et expose analytique de l'ensemble des travaux executes sur cet astre depuis 1659. Paris: Hermann & Cie, 1930.
- Audouard, J., Poulet, F., Vincendon, M., Milliken, R.E., Jouglet, D., Bibring, J.P., Gondet, B., Langevin, Y., 2014. Water in the Martian regolith from OMEGA/Mars Express. *Journal of Geophysical Research: Planets* 119, 1969–1989. URL: <http://agupubs.onlinelibrary.wiley.com/doi/abs/10.1002/2014JE004649>, doi:10.1002/2014JE004649. _eprint: <https://onlinelibrary.wiley.com/doi/pdf/10.1002/2014JE004649>.
- Balme, M.R., Whelley, P.L., Greeley, R., 2003. Mars: Dust devil track survey in Argyre Planitia and Hellas Basin. *Journal of Geophysical Research: Planets* 108, 5086. doi:10.1029/2003JE002096.
- Battalio, M., Wang, H., 2019. The Aonia-Solis-Valles dust storm track in the southern hemisphere of Mars. *Icarus* 321, 367–378. URL: <https://www.sciencedirect.com/science/article/pii/S0019103518305402>, doi:10.1016/j.icarus.2018.10.026.
- Battalio, M., Wang, H., 2021. The Mars Dust Activity Database (MDAD): A comprehensive statistical study of dust storm sequences. *Icarus* 354, 114059. URL: <https://www.sciencedirect.com/science/article/pii/S001910352030405X>, doi:10.1016/j.icarus.2020.114059.
- Bell, J.F., McSween, H.Y., Crisp, J.A., Morris, R.V., Murchie, S.L., Bridges, N.T., Johnson, J.R., Britt, D.T., Golombek, M.P., Moore, H.J., Ghosh, A., Bishop, J.L., Anderson, R.C., Brückner, R., Economou, T., Greenwood, J.P., Gunnlaugsson, H.P., Hargraves, R.M., Hviid, S., Knudsen, J.M., Madsen, M.B., Reid, R., Rieder, R., Soderblom, L., 2000. Mineralogic and compositional properties of Martian soil and dust: Results from Mars Pathfinder. *Journal of Geophysical Research: Planets* 105, 1721–1756. doi:10.1029/1999JE001060.
- Bertrand, T., Kahre, M., Urata, R., Määttä, A., Montmessin, F., Wilson, R., Wolff, M., 2022. Impact of the coagulation of dust particles on mars during the 2018 global dust storm. *Icarus* 388, 115239. URL: <https://www.sciencedirect.com/science/article/pii/S0019103522003323>, doi:https://doi.org/10.1016/j.icarus.2022.115239.
- Bertrand, T., Wilson, R.J., Kahre, M.A., Urata, R., Kling, A., 2020. Simulation of the 2018 Global Dust Storm on Mars Using the NASA Ames Mars GCM: A Multitracer Approach. *Journal of Geophysical Research: Planets* 125, e2019JE006122. URL: <http://onlinelibrary.wiley.com/doi/abs/10.1029/2019JE006122>, doi:10.1029/2019JE006122. _eprint: <https://agupubs.onlinelibrary.wiley.com/doi/pdf/10.1029/2019JE006122>.
- Bibring, J.P., Soufflot, A., Berthé, M., Langevin, Y., Gondet, B., Drossart, P., Bouyé, M., Combes, M., Puget, P., Semery, A., Bellucci, G., Formisano, V., Moroz, V., Kottsov, V., Bonello, G., Erard, S., Forni, O., Gendrin, A., Manaud, N., Poulet, F., Poulleau, G., Encrenaz, T., Fouchet, T., Melchiorri, R., Altieri, F., Ignatiev, N., Titov, D., Zasova, L., Coradini, A., Capacionni, F., Cerroni, P., Fonti, S., Mangold, N., Pinet, P., Schmitt, B., Sotin, C., Hauber, E., Hoffmann, H., Jaumann, R., Keller, U., Arvidson, R., Mustard, J., Forget, F., 2004. OMEGA: Observatoire pour la Minéralogie, l'Eau, les Glaces et l'Activité. *ESA* 1240, 37–49. URL: <https://ui.adsabs.harvard.edu/abs/2004ESASP1240...37B>. conference Name: Mars Express: the Scientific Payload ADS Bibcode: 2004ESASP1240...37B.
- Cantor, B.A., 2007. MOC observations of the 2001 Mars planet-encircling dust storm. *Icarus* 186, 60–96. URL: <https://www.sciencedirect.com/science/article/pii/S0019103506002855>, doi:10.1016/j.icarus.2006.08.019.
- Cantor, B.A., James, P.B., Caplinger, M., Wolff, M.J., 2001. Martian dust storms: 1999 Mars Orbiter Camera observations. *Journal of Geophysical Research: Planets* 106, 23653–23687. URL: <http://onlinelibrary.wiley.com/doi/abs/10.1029/2000JE001310>, doi:10.1029/2000JE001310. _eprint: <https://agupubs.onlinelibrary.wiley.com/doi/pdf/10.1029/2000JE001310>.
- Cantor, B.A., Kanak, K.M., Edgett, K.S., 2006. Mars Orbiter Camera observations of Martian dust devils and their tracks (September 1997 to January 2006) and evaluation of theoretical vortex models. *Journal of Geophysical Research: Planets* 111, E12002. doi:10.1029/2006JE002700.
- Clancy, R.T., Sandor, B.J., Wolff, M.J., Smith, M.D., Lefèvre, F., Madeleine, J.B., Forget, F., Murchie, S.L., Seelos, F.P., Seelos, K.D., Nair, H.A., Toigo, A.D., Humm, D., Kass, D.M., Kleinböhl, A., Heavens, N., 2012. Extensive MRO CRISM observations of 1.27 μm O_2 airglow in Mars polar night and their comparison to MRO MCS temperature profiles and LMD GCM simulations. *Journal of Geophysical Research: Planets* 117, E00J10. doi:10.1029/2011JE004018.
- Clancy, R.T., Wolff, M.J., Christensen, P.R., 2003. Mars aerosol studies with the MGS TES emission phase function observations: Optical depths, particle sizes, and ice cloud types versus latitude and solar longitude. *Journal of Geophysical Research: Planets* 108, 5098. doi:10.1029/2003JE002058.
- Clancy, R.T., Wolff, M.J., Whitney, B.A., Cantor, B.A., Smith, M.D., McConnochie, T.H., 2010. Extension of atmospheric dust loading to high altitudes during the 2001 Mars dust storm: MGS TES limb observations. *Icarus* 207, 98–109. URL: <https://www.sciencedirect.com/science/article/pii/S0019103509004278>, doi:10.1016/j.icarus.2009.10.011.
- D'Aversa, E., Oliva, F., Altieri, F., Sindoni, G., Carrozzo, F.G., Bellucci, G., Forget, F., Geminale, A., Mahieux, A., Aoki, S., Amoroso, M., 2022. Vertical distribution of dust in the martian atmosphere: OMEGA/MEx limb observations. *Icarus* 371, 114702. URL: <https://www.sciencedirect.com/science/article/pii/S0019103521003572>, doi:10.1016/j.icarus.2021.114702.
- Dundas, C.M., 2020. An aeolian grainflow model for Martian Recurring Slope Lineae. *Icarus* 343, 113681. URL: <https://www.sciencedirect.com/science/article/pii/S0019103520300725>, doi:10.1016/j.icarus.2020.113681.
- Dundas, C.M., McEwen, A.S., Chojnacki, M., Milazzo, M.P., Byrne, S., McElwaine, J.N., Urso, A., 2017. Granular flows at recurring slope lineae on Mars indicate a limited role for liquid water. *Nature Geoscience* 10, 903–907. URL: <http://www.nature.com/articles/s41561-017-0012-5>, doi:10.1038/s41561-017-0012-5. number: 12 Publisher: Nature Publishing Group.
- Encrenaz, T., Melchiorri, R., Fouchet, T., Drossart, P., Lellouch, E., Gondet, B., Bibring, J.P., Langevin, Y., Titov, D., Ignatiev, N., Forget, F., 2005. A mapping of martian water sublimation during early northern summer using OMEGA/Mars Express. *Astronomy & Astrophysics* 441, L9–L12. doi:10.1051/0004-6361:200500171.
- Forget, F., Hourdin, F., Fournier, R., Hourdin, C., Talagrand, O., Collins, M., Lewis, S.R., Read, P.L., Huot, J.P., 1999. Improved general circulation models of the Martian atmosphere from the surface to above 80 km. *Journal of Geophysical Research: Planets* 104, 24155–24175. URL: <http://onlinelibrary.wiley.com/doi/abs/10.1029/1999JE001025>, doi:10.1029/1999JE001025. _eprint: <https://agupubs.onlinelibrary.wiley.com/doi/pdf/10.1029/1999JE001025>.
- Forget, F., Hourdin, F., Talagrand, O., 1998. CO2 snowfall on Mars: Simulation with a General Circulation Model. *Icarus* 131, 302–316. URL: <https://www.sciencedirect.com/science/article/pii/S0019103597958747>, doi:10.1006/icar.1997.5874.
- Forget, F., Spiga, A., Dolla, B., Vinatier, S., Melchiorri, R., Drossart, P., Gendrin, A., Bibring, J.P., Langevin, Y., Gondet, B., 2007. Remote sensing of surface pressure on Mars with the Mars Express/OMEGA spectrometer: 1. Retrieval method. *Journal of Geophysical Research: Planets* 112. URL: <http://agupubs.onlinelibrary.wiley.com/doi/abs/10.1029/2006JE002871>, doi:10.1029/2006JE002871. _eprint: <https://onlinelibrary.wiley.com/doi/pdf/10.1029/2006JE002871>.
- Geissler, P.E., 2005. Three decades of Martian surface changes. *Journal of Geophysical Research: Planets* 110. URL: <https://onlinelibrary.wiley.com/doi/abs/10.1029/2004JE002345>, doi:10.1029/2004JE002345. _eprint: <https://onlinelibrary.wiley.com/doi/pdf/10.1029/2004JE002345>.
- Goetz, W., Bertelsen, P., Binau, C.S., Gunnlaugsson, H.P., Hviid, S.F., Kinch, K.M., Madsen, D.E., Madsen, M.B., Olsen, M., Gellert, R., Klingelhöfer, G., Ming, D.W., Morris, R.V., Rieder, R., Rodionov, D.S.,

- de Souza, P.A., Schröder, C., Squyres, S.W., Wdowiak, T., Yen, A., 2005. Indication of drier periods on Mars from the chemistry and mineralogy of atmospheric dust. *Nature* 436, 62–65. doi:10.1038/nature03807.
- Guzewich, S.D., Lemmon, M., Smith, C.L., Martínez, G., de Vicente-Retortillo, A., Newman, C.E., Baker, M., Campbell, C., Cooper, B., Gómez-Elvira, J., Harri, A.M., Hassler, D., Martin-Torres, F.J., McConnochie, T., Moores, J.E., Kahanpää, H., Khayat, A., Richardson, M.I., Smith, M.D., Sullivan, R., de la Torre Juárez, M., Vasavada, A.R., Viúdez-Moreiras, D., Zeitlin, C., Zorzano Mier, M.P., 2019. Mars Science Laboratory Observations of the 2018/Mars Year 34 Global Dust Storm. *Geophysical Research Letters* 46, 71–79. URL: <https://onlinelibrary.wiley.com/doi/abs/10.1029/2018GL080839>, doi:10.1029/2018GL080839. _eprint: <https://onlinelibrary.wiley.com/doi/pdf/10.1029/2018GL080839>.
- Haberle, R.M., Leovy, C.B., Pollack, J.B., 1982. Some effects of global dust storms on the atmospheric circulation of Mars. *Icarus* 50, 322–367. URL: <https://www.sciencedirect.com/science/article/pii/0019103582901294>, doi:https://doi.org/10.1016/0019-1035(82)90129-4.
- Heavens, N.G., Kass, D.M., Shirley, J.H., 2019. Dusty Deep Convection in the Mars Year 34 Planet-Encircling Dust Event. *Journal of Geophysical Research: Planets* 124, 2863–2892. URL: <https://onlinelibrary.wiley.com/doi/abs/10.1029/2019JE006110>, doi:10.1029/2019JE006110. _eprint: <https://onlinelibrary.wiley.com/doi/pdf/10.1029/2019JE006110>.
- Kahre, M.A., Hollingsworth, J.L., Haberle, R.M., Murphy, J.R., 2008. Investigations of the variability of dust particle sizes in the martian atmosphere using the nasa Ames general circulation model. *Icarus* 195, 576–597. URL: <https://www.sciencedirect.com/science/article/pii/S0019103508000614>, doi:https://doi.org/10.1016/j.icarus.2008.01.023.
- Kahre, M.A., Murphy, J.R., Haberle, R.M., Montmessin, F., Schaeffer, J., 2005. Simulating the Martian dust cycle with a finite surface dust reservoir. *Geophysical Research Letters* 32. URL: <http://onlinelibrary.wiley.com/doi/abs/10.1029/2005GL023495>, doi:10.1029/2005GL023495. _eprint: <https://agupubs.onlinelibrary.wiley.com/doi/pdf/10.1029/2005GL023495>.
- Kahre, M.A., Vines, S.K., Haberle, R.M., Hollingsworth, J.L., 2013. The early Martian atmosphere: Investigating the role of the dust cycle in the possible maintenance of two stable climate states. *Journal of Geophysical Research: Planets* 118, 1388–1396. doi:10.1002/jgre.20099.
- Kass, D.M., Kleinböhl, A., McCleese, D.J., Schofield, J.T., Smith, M.D., 2016. Interannual similarity in the Martian atmosphere during the dust storm season. *Geophysical Research Letters* 43, 6111–6118. URL: <https://agupubs.onlinelibrary.wiley.com/doi/abs/10.1002/2016GL068978>, doi:10.1002/2016GL068978. _eprint: <https://agupubs.onlinelibrary.wiley.com/doi/pdf/10.1002/2016GL068978>.
- Kieffer, H.H., Titus, T.N., 2001. TES Mapping of Mars' North Seasonal Cap. *Icarus* 154, 162–180. URL: <https://www.sciencedirect.com/science/article/pii/S0019103501966709>, doi:10.1006/icar.2001.6670.
- Kieffer, H.H., Titus, T.N., Mullins, K.F., Christensen, P.R., 2000. Mars south polar spring and summer behavior observed by TES: Seasonal cap evolution controlled by frost grain size. *Journal of Geophysical Research: Planets* 105, 9653–9699. URL: <http://onlinelibrary.wiley.com/doi/abs/10.1029/1999JE001136>, doi:10.1029/1999JE001136. _eprint: <https://agupubs.onlinelibrary.wiley.com/doi/pdf/10.1029/1999JE001136>.
- Langevin, Y., Bibring, J.P., Montmessin, F., Forget, F., Vincendon, M., Douté, S., Poulet, F., Gondet, B., 2007. Observations of the south seasonal cap of Mars during recession in 2004–2006 by the OMEGA visible/near-infrared imaging spectrometer on board Mars Express. *Journal of Geophysical Research: Planets* 112. URL: <http://agupubs.onlinelibrary.wiley.com/doi/abs/10.1029/2006JE002841>, doi:10.1029/2006JE002841. _eprint: <https://onlinelibrary.wiley.com/doi/pdf/10.1029/2006JE002841>.
- Lasue, J., Meslin, P.Y., Cousin, A., Forni, O., Anderson, R., Beck, P., Clegg, S.M., Dehouck, E., Frydenvang, J., Gasda, P., Gasnault, O., Hausrath, E., Le Mouélic, S., Maurice, S., Pilleri, P., Rapin, W., Wiens, R.C., 2022. Comparison of Dust Between Gale and Jezero 2678, 1758. URL: <https://ui.adsabs.harvard.edu/abs/2022LPICo2678.1758L>. conference Name: LPI Contributions ADS Bibcode: 2022LPICo2678.1758L.
- Lemmon, M.T., Guzewich, S.D., McConnochie, T., de Vicente-Retortillo, A., Martínez, G., Smith, M.D., Bell III, J.F., Wellington, D., Jacob, S., 2019. Large Dust Aerosol Sizes Seen During the 2018 Martian Global Dust Event by the Curiosity Rover. *Geophysical Research Letters* 46, 9448–9456. URL: <http://onlinelibrary.wiley.com/doi/abs/10.1029/2019GL084407>, doi:10.1029/2019GL084407. _eprint: <https://agupubs.onlinelibrary.wiley.com/doi/pdf/10.1029/2019GL084407>.
- Lemmon, M.T., Wolff, M.J., Bell, J.F., Smith, M.D., Cantor, B.A., Smith, P.H., 2015. Dust aerosol, clouds, and the atmospheric optical depth record over 5 Mars years of the Mars Exploration Rover mission. *Icarus* 251, 96–111. URL: <https://www.sciencedirect.com/science/article/pii/S0019103514001559>, doi:10.1016/j.icarus.2014.03.029.
- Madeleine, J.B., Forget, F., Spiga, A., Wolff, M.J., Montmessin, F., Vincendon, M., Jouglet, D., Gondet, B., Bibring, J.P., Langevin, Y., Schmitt, B., 2012. Aphelion water-ice cloud mapping and property retrieval using the OMEGA imaging spectrometer onboard Mars Express. *Journal of Geophysical Research: Planets* 117. URL: <http://onlinelibrary.wiley.com/doi/abs/10.1029/2011JE003940>, doi:10.1029/2011JE003940. _eprint: <https://onlinelibrary.wiley.com/doi/pdf/10.1029/2011JE003940>.
- Martin, L.J., Zurek, R.W., 1993. An analysis of the history of dust activity on Mars. *Journal of Geophysical Research: Planets* 98, 3221–3246. URL: <http://onlinelibrary.wiley.com/doi/abs/10.1029/92JE02937>, doi:10.1029/92JE02937. _eprint: <https://agupubs.onlinelibrary.wiley.com/doi/pdf/10.1029/92JE02937>.
- McEwen, A.S., Dundas, C.M., Mattson, S.S., Toigo, A.D., Ojha, L., Wray, J.J., Chojnacki, M., Byrne, S., Murchie, S.L., Thomas, N., 2014. Recurring slope lineae in equatorial regions of Mars. *Nature Geoscience* 7, 53–58. doi:10.1038/ngeo2014.
- McEwen, A.S., Ojha, L., Dundas, C.M., Mattson, S.S., Byrne, S., Wray, J.J., Cull, S.C., Murchie, S.L., Thomas, N., Gulick, V.C., 2011. Seasonal Flows on Warm Martian Slopes. *Science* 333, 740. URL: <https://ui.adsabs.harvard.edu/abs/2011Sci...333..740M>, doi:10.1126/science.1204816. ADS Bibcode: 2011Sci...333..740M.
- McEwen, A.S., Schaefer, E.I., Dundas, C.M., Sutton, S.S., Tamppari, L.K., Chojnacki, M., 2021. Mars: Abundant Recurring Slope Lineae (RSL) Following the Planet-Encircling Dust Event (PEDE) of 2018. *Journal of Geophysical Research: Planets* 126, e2020JE006575. URL: <http://onlinelibrary.wiley.com/doi/abs/10.1029/2020JE006575>, doi:10.1029/2020JE006575. _eprint: <https://agupubs.onlinelibrary.wiley.com/doi/pdf/10.1029/2020JE006575>.
- Millour, E., Forget, F., Spiga, A., Vals, M., Zakharov, V., Montabone, L., Lefèvre, F., Montmessin, F., Chaufray, J.Y., López-Valverde, M.A., González-Galindo, F., Lewis, S.R., Read, P.L., Desjean, M.C., Cipriani, F., MCD Development Team, 2018. The Mars Climate Database (version 5.3). URL: <https://ui.adsabs.harvard.edu/abs/2018fmee.confE..68M>. .68M. conference Name: From Mars Express to ExoMars Pages: 68 ADS Bibcode: 2018fmee.confE..68M.
- Montabone, L., Forget, F., Millour, E., Wilson, R.J., Lewis, S.R., Cantor, B., Kass, D., Kleinböhl, A., Lemmon, M.T., Smith, M.D., Wolff, M.J., 2015. Eight-year climatology of dust optical depth on Mars. *Icarus* 251, 65–95. URL: <https://www.sciencedirect.com/science/article/pii/S0019103515000044>, doi:10.1016/j.icarus.2014.12.034.
- Montabone, L., Spiga, A., Kass, D.M., Kleinböhl, A., Forget, F., Millour, E., 2020. Martian Year 34 Column Dust Climatology from Mars Climate Sounder Observations: Reconstructed Maps and Model Simulations. *Journal of Geophysical Research: Planets* 125, e2019JE006111. URL: <https://agupubs-onlinelibrary-wiley-com.insu.bib.cnrs.fr/doi/10.1029/2019JE006111>, doi:10.1029/2019JE006111. publisher: John Wiley & Sons, Ltd.
- Munaretto, G., Pajola, M., Lucchetti, A., Cremonese, G., Simioni, E., Re, C., Bertoli, S., Tornabene, L., McEwen, A.S., Becerra, P., Rangarajan, V.G., Valantinas, A., Pommerol, A., Thomas, N., Portyankina, G., 2022. Multiband photometry of Martian Recurring Slope Lineae (RSL) and dust-removed features at Horowitz crater, Mars from TGO/CaSSIS color observations. *Planetary and Space Science* 214, 105443. URL: <https://www.sciencedirect.com/science/article/pii/S0032063322000290>, doi:10.1016/j.pss.2022.105443.

- Määttänen, A., Fouchet, T., Forni, O., Forget, F., Savijärvi, H., Gondet, B., Melchiorri, R., Langevin, Y., Formisano, V., Giuranna, M., Bibring, J.P., 2009. A study of the properties of a local dust storm with Mars Express OMEGA and PFS data. *Icarus* 201, 504–516. URL: <https://www.sciencedirect.com/science/article/pii/S0019103509000475>, doi:10.1016/j.icarus.2009.01.024.
- Newman, C.E., Richardson, M.I., 2015. The impact of surface dust source exhaustion on the martian dust cycle, dust storms and interannual variability, as simulated by the MarsWRF General Circulation Model. *Icarus* 257, 47–87. URL: <https://www.sciencedirect.com/science/article/pii/S0019103515001311>, doi:10.1016/j.icarus.2015.03.030.
- Ody, A., Poulet, F., Langevin, Y., Bibring, J.P., Bellucci, G., Altieri, F., Gondet, B., Vincendon, M., Carter, J., Manaud, N., 2012. Global maps of anhydrous minerals at the surface of Mars from OMEGA/MEx. *Journal of Geophysical Research: Planets* 117. URL: <https://onlinelibrary.wiley.com/doi/abs/10.1029/2012JE004117>, doi:10.1029/2012JE004117. _eprint: <https://onlinelibrary.wiley.com/doi/pdf/10.1029/2012JE004117>.
- Oliva, F., Geminale, A., D'Aversa, E., Altieri, F., Bellucci, G., Carrozzo, F.G., Sindoni, G., Grassi, D., 2018. Properties of a Martian local dust storm in Atlantis Chaos from OMEGA/MEX data. *Icarus* 300, 1–11. doi:10.1016/j.icarus.2017.07.034, arXiv:1709.00986.
- Rannou, P., Perrier, S., Bertaux, J.L., Montmessin, F., Korabiev, O., Rébéac, A., 2006. Dust and cloud detection at the Mars limb with UV scattered sunlight with SPICAM. *Journal of Geophysical Research: Planets* 111. URL: <https://onlinelibrary.wiley.com/doi/abs/10.1029/2006JE002693>, doi:10.1029/2006JE002693. _eprint: <https://onlinelibrary.wiley.com/doi/pdf/10.1029/2006JE002693>.
- Schaefer, E.I., McEwen, A.S., Sutton, S.S., 2019. A case study of recurring slope lineae (RSL) at Tivat crater: Implications for RSL origins. *Icarus* 317, 621–648. URL: <https://www.sciencedirect.com/science/article/pii/S0019103518300137>, doi:10.1016/j.icarus.2018.07.014.
- Schmidt, F., Andrieu, F., Costard, F., Kocifaj, M., Meresescu, A.G., 2017. Formation of recurring slope lineae on Mars by rarefied gas-triggered granular flows. *Nature Geoscience* 10, 270–273. URL: <http://www.nature.com/articles/ngeo2917>, doi:10.1038/ngeo2917. number: 4 Publisher: Nature Publishing Group.
- Smith, M.D., 2004. Interannual variability in TES atmospheric observations of Mars during 1999–2003. *Icarus* 167, 148–165. URL: <https://www.sciencedirect.com/science/article/pii/S0019103503002872>, doi:10.1016/j.icarus.2003.09.010.
- Smith, M.D., 2008. Spacecraft Observations of the Martian Atmosphere. URL: <https://www.annualreviews.org/doi/epdf/10.1146/annurev.earth.36.031207.124334>, doi:10.1146/annurev.earth.36.031207.124334.
- Smith, M.D., Wolff, M.J., Clancy, R.T., Kleinböhl, A., Murchie, S.L., 2013. Vertical distribution of dust and water ice aerosols from CRISM limb-geometry observations. *Journal of Geophysical Research: Planets* 118, 321–334. doi:10.1002/jgre.20047.
- Spiga, A., Faure, J., Madeleine, J.B., Määttänen, A., Forget, F., 2013. Rocket dust storms and detached dust layers in the Martian atmosphere. *Journal of Geophysical Research: Planets* 118, 746–767. URL: <https://onlinelibrary.wiley.com/doi/abs/10.1002/jgre.20046>, doi:10.1002/jgre.20046. _eprint: <https://onlinelibrary.wiley.com/doi/pdf/10.1002/jgre.20046>.
- Spiga, A., Forget, F., Dolla, B., Vianier, S., Melchiorri, R., Drossart, P., Gendrin, A., Bibring, J.P., Langevin, Y., Gondet, B., 2007. Remote sensing of surface pressure on Mars with the Mars Express/OMEGA spectrometer: 2. Meteorological maps. *Journal of Geophysical Research: Planets* 112. URL: <http://onlinelibrary.wiley.com/doi/abs/10.1029/2006JE002870>, doi:10.1029/2006JE002870. _eprint: <https://agupubs.onlinelibrary.wiley.com/doi/pdf/10.1029/2006JE002870>.
- Stillman, D.E., 2018. Chapter 2 - Unraveling the Mysteries of Recurring Slope Lineae, in: Soare, R.J., Conway, S.J., Clifford, S.M. (Eds.), *Dynamic Mars*. Elsevier, pp. 51–85. URL: <https://www.sciencedirect.com/science/article/pii/B978012813018600029>, doi:10.1016/B978-0-12-813018-6.00002-9.
- Stillman, D.E., Grimm, R.E., 2018. Two pulses of seasonal activity in martian southern mid-latitude recurring slope lineae (RSL). *Icarus* 302, 126–133. URL: <https://www.sciencedirect.com/science/article/pii/S0019103517303226>, doi:10.1016/j.icarus.2017.10.026.
- Stillman, D.E., Michaels, T.I., Grimm, R.E., Hanley, J., 2016. Observations and modeling of northern mid-latitude recurring slope lineae (RSL) suggest recharge by a present-day martian briny aquifer. *Icarus* 265, 125–138. URL: <https://www.sciencedirect.com/science/article/pii/S001910351500473X>, doi:10.1016/j.icarus.2015.10.007.
- Strausberg, M.J., Wang, H., Richardson, M.I., Ewald, S.P., Toigo, A.D., 2005. Observations of the initiation and evolution of the 2001 Mars global dust storm. *Journal of Geophysical Research: Planets* 110. URL: <https://onlinelibrary.wiley.com/doi/abs/10.1029/2004JE002361>, doi:10.1029/2004JE002361. _eprint: <https://onlinelibrary.wiley.com/doi/pdf/10.1029/2004JE002361>.
- Szwast, M.A., Richardson, M.I., Vasavada, A.R., 2006. Surface dust redistribution on Mars as observed by the Mars Global Surveyor and Viking orbiters. *Journal of Geophysical Research: Planets* 111. URL: <http://agupubs.onlinelibrary.wiley.com/doi/abs/10.1029/2005JE002485>, doi:10.1029/2005JE002485. _eprint: <https://onlinelibrary.wiley.com/doi/pdf/10.1029/2005JE002485>.
- Sánchez-Lavega, A., Erkoreka, A., Hernández-Bernal, J., del Río-Gaztelurrutia, T., García-Morales, J., Ordoñez-Etxebarria, I., Cardesín-Moinelo, A., Titov, D., Wood, S., Tirsch, D., Hauber, E., Matz, K.D., 2022. Cellular patterns and dry convection in textured dust storms at the edge of Mars North Polar Cap. *Icarus* 387, 115183. URL: <https://www.sciencedirect.com/science/article/pii/S0019103522002846>, doi:10.1016/j.icarus.2022.115183.
- Thomas, P.C., Gierasch, P., Sullivan, R., Miller, D.S., Alvarez del Castillo, E., Cantor, B., Mellon, M.T., 2003. Mesoscale linear streaks on Mars: environments of dust entrainment. *Icarus* 162, 242–258. URL: <https://www.sciencedirect.com/science/article/pii/S0019103503000289>, doi:10.1016/S0019-1035(03)00028-9.
- Titov, D.V., Fedorova, A.A., Haus, R., 2000. A new method of remote sounding of the Martian aerosols by means of spectroscopy in the 2.7 μm CO_2 band. *Planetary and Space Science* 48, 67–74. URL: <https://www.sciencedirect.com/science/article/pii/S003206339900077X>, doi:10.1016/S0032-0633(99)00077-X.
- Titus, T.N., 2005. Mars Polar Cap Edges Tracked over 3 Full Mars Years, 1993. URL: <https://ui.adsabs.harvard.edu/abs/2005LPI....36.1993T>. conference Name: 36th Annual Lunar and Planetary Science Conference ADS Bibcode: 2005LPI....36.1993T.
- Toon, O.B., Pollack, J.B., Sagan, C., 1977. Physical Properties of the Particles Composing the Martian Dust Storm of 1971–1972. *Icarus* 30, 663–696. doi:10.1016/0019-1035(77)90088-4.
- Vincendon, M., Audouard, J., Altieri, F., Ody, A., 2015. Mars Express measurements of surface albedo changes over 2004–2010. *Icarus* 251, 145–163. URL: <https://www.sciencedirect.com/science/article/pii/S0019103514005764>, doi:10.1016/j.icarus.2014.10.029.
- Vincendon, M., Langevin, Y., Poulet, F., Bibring, J.P., Gondet, B., 2007. Recovery of surface reflectance spectra and evaluation of the optical depth of aerosols in the near-IR using a Monte Carlo approach: Application to the OMEGA observations of high-latitude regions of Mars. *Journal of Geophysical Research: Planets* 112, E08S13. doi:10.1029/2006JE002845, arXiv:1103.0384.
- Vincendon, M., Langevin, Y., Poulet, F., Bibring, J.P., Gondet, B., Jouglet, D., Omega Team, 2008. Dust aerosols above the south polar cap of Mars as seen by OMEGA. *Icarus* 196, 488–505. doi:10.1016/j.icarus.2007.11.034, arXiv:1103.0854.
- Vincendon, M., Langevin, Y., Poulet, F., Pommerol, A., Wolff, M., Bibring, J.P., Gondet, B., Jouglet, D., 2009. Yearly and seasonal variations of low albedo surfaces on Mars in the OMEGA/MEx dataset: Constraints on aerosols properties and dust deposits. *Icarus* 200, 395–405. URL: <https://www.sciencedirect.com/science/article/pii/S0019103508004387>, doi:10.1016/j.icarus.2008.12.012.
- Vincendon, M., Pilorget, C., Carter, J., Scherbinine, A., 2019. Observational evidence for a dry dust-wind origin of Mars seasonal dark flows. *Icarus* 325, 115–127. URL: <https://www.sciencedirect.com/science/article/pii/S0019103518305712>, doi:10.1016/j.icarus.2019.02.024.

- Vincendon, M., Pilorget, C., Gondet, B., Murchie, S., Bibring, J.P., 2011. New near-IR observations of mesospheric CO₂ and H₂O clouds on Mars. *Journal of Geophysical Research: Planets* 116. URL: <http://onlinelibrary.wiley.com/doi/abs/10.1029/2011JE003827>, doi:10.1029/2011JE003827. _eprint: <https://onlinelibrary.wiley.com/doi/pdf/10.1029/2011JE003827>.
- Wang, H., Richardson, M.I., 2015. The origin, evolution, and trajectory of large dust storms on Mars during Mars years 24–30 (1999–2011). *Icarus* 251, 112–127. URL: <https://www.sciencedirect.com/science/article/pii/S0019103513004624>, doi:10.1016/j.icarus.2013.10.033.
- Wolff, M.J., Clancy, R.T., 2003. Constraints on the size of Martian aerosols from Thermal Emission Spectrometer observations. *Journal of Geophysical Research: Planets* 108. URL: <https://onlinelibrary.wiley.com/doi/abs/10.1029/2003JE002057>, doi:10.1029/2003JE002057. _eprint: <https://onlinelibrary.wiley.com/doi/pdf/10.1029/2003JE002057>.
- Wolff, M.J., Smith, M.D., Clancy, R.T., Spanovich, N., Whitney, B.A., Lemmon, M.T., Bandfield, J.L., Banfield, D., Ghosh, A., Landis, G., Christensen, P.R., Bell III, J.F., Squyres, S.W., 2006. Constraints on dust aerosols from the Mars Exploration Rovers using MGS overflights and Mini-TES. *Journal of Geophysical Research: Planets* 111. URL: <https://onlinelibrary.wiley.com/doi/abs/10.1029/2006JE002786>, doi:10.1029/2006JE002786. _eprint: <https://onlinelibrary.wiley.com/doi/pdf/10.1029/2006JE002786>.
- Zurek, R.W., Martin, L.J., 1993. Interannual variability of planet-encircling dust storms on Mars. *Journal of Geophysical Research: Planets* 98, 3247–3259. URL: <http://onlinelibrary.wiley.com/doi/abs/10.1029/92JE02936>, doi:10.1029/92JE02936. _eprint: <https://agupubs.onlinelibrary.wiley.com/doi/pdf/10.1029/92JE02936>.